The Astrophysical Journal, 923:28 (20pp), 2021 December 10 https://doi.org/10.3847/1538-4357/ac2510

GASP and MaNGA Surveys Shed Light on the Enigma of the Gas Metallicity Gradients in Disk Galaxies

Andrea Franchetto[1,2], Matilde Mingozzi[3], Bianca M. Poggianti[2], Benedetta Vulcani[2], Cecilia Bacchini[2], Marco Gullieuszik[2], Alessia Moretti[2], Neven Tomičić[2], and Jacopo Fritz[4]
[1] Dipartimento di Fisica e Astronomia "Galileo Galilei," Università di Padova, vicolo dell'Osservatorio 3, I-35122, Padova, Italy; andrea.franchetto@phd.unipd.it
[2] INAF—Astronomical Observatory of Padova, vicolo dell'Osservatorio 5, I-35122 Padova, Italy
[3] Space Telescope Science Institute, 3700 San Martin Drive, Baltimore, MD 21218, USA
[4] Instituto de Radioastronomía y Astrofísica, UNAM, Campus Morelia, A.P. 3-72, C.P. 58089, México
Received 2021 April 28; revised 2021 August 27; accepted 2021 September 6; published 2021 December 8

Abstract

Making use of both MUSE observations of 85 galaxies from the survey GASP (GAs Stripping Phenomena in galaxies with MUSE) and a large sample from MaNGA (Mapping Nearby Galaxies at Apache Point Observatory survey), we investigate the distribution of gas metallicity gradients as a function of stellar mass for local cluster and field galaxies. Overall, metallicity profiles steepen with increasing stellar mass up to $10^{10.3}\,M_{\odot}$ and flatten out at higher masses. Combining the results from the metallicity profiles and the stellar mass surface density gradients, we propose that the observed steepening is a consequence of local metal enrichment due to in situ star formation during the inside-out formation of disk galaxies. The metallicity gradient−stellar mass relation is characterized by a rather large scatter, especially for $10^{9.8} < M_{\star}/M_{\odot} < 10^{10.5}$, and we demonstrate that metallicity gradients anti-correlate with the galaxy gas fraction. Focusing on the galaxy environment, at any given stellar mass, cluster galaxies have systematically flatter metallicity profiles than their field counterparts. Many subpopulations coexist in clusters: galaxies with shallower metallicity profiles appear to have fallen into their present host halo sooner and have experienced the environmental effects for a longer time than cluster galaxies with steeper metallicity profiles. Recent galaxy infallers, like galaxies currently undergoing ram pressure stripping, show metallicity gradients more similar to those of field galaxies, suggesting they have not felt the effect of the cluster yet.

Unified Astronomy Thesaurus concepts: Galaxy disks (589); Galaxy clusters (584); Field galaxies (533); Metallicity (1031); Galaxy chemical evolution (580)

Supporting material: data behind figure, figure set, machine-readable tables

1. Introduction

Spiral galaxies are thought to form inside-out: gas that collapses in the center cools in a short timescale and stars form at an accelerated pace with respect to the outer regions (Larson 1976). Metals, produced by stellar nucleosynthesis, are injected into the interstellar medium (ISM) during the lifetime of stars, producing the gas chemical enrichment. The evolution of a galaxy is then regulated by the possible increase of gas content (either through cold gas accretion or by merging with nearby satellites), by the ability of the gas to form new stars, and by the possible enriched gas ejection/redistribution due to the stellar and/or active galactic nuclei feedback (see Maiolino & Mannucci 2019 for a review). In addition, galaxies suffer from environmental effects that can shape their properties, such as morphology, gas fraction, and star formation rate (SFR). The metallicity of galaxies stems from all these ingredients and, therefore, is a fundamental tracer to explore galaxy evolution.

The global chemical abundance of the gas in disk galaxies linearly increases with stellar mass according to the mass–metallicity relation (MZR), reaching an asymptotic value at the highest masses (Tremonti et al. 2004; Kewley & Ellison 2008; Sánchez et al. 2013; Blanc et al. 2019). The secondary dependence of the gas metallicity on the SFR, i.e., at a given stellar mass high-SFR galaxies have lower chemical abundances (Mannucci et al. 2010; Cresci et al. 2019), brought to light the anti-correlation between the ISM metallicity and the gas fraction (De Rossi et al. 2016; Brown et al. 2018), which is interpreted as an effect of dilution due to metal-poor gas accretion (De Lucia et al. 2020). Also the galaxy environment plays a role, as cluster galaxies are slightly more metal-rich with respect to field counterparts at a fixed stellar mass (Maier et al. 2019; Franchetto et al. 2020), though such enrichment might be due to a local density effect (Cooper et al. 2008; Ellison et al. 2009; Peng & Maiolino 2014; Wu et al. 2017).

A way of understanding the mechanisms of formation and evolution of galaxies is investigating the radial distribution of the ISM metallicity across galaxy disks. The first evidence of negative abundance gradients in a small sample of spiral galaxies goes back to Searle (1971), and was confirmed by many subsequent works (Pagel & Edmunds 1981; Zaritsky et al. 1994; Deharveng et al. 2000; Magrini et al. 2007; Bresolin 2007; Berg et al. 2013, 2015). The decrease of the metallicity as a function of the galactocentric distance is often interpreted as the natural result of the inside-out formation of galaxy disks (Prantzos & Boissier 2000). In addition, signs of flattening of the metallicity profile are found beyond R_{25}, (Bresolin 2015). That said, positive metallicity gradients are measured in some high-redshift galaxies and in merging systems, as a consequence of metal-poor gas accretion and mixing of the gas (Cresci et al. 2010; Rupke et al. 2010; Rich et al. 2012).

The advent of spectroscopy based on integral-field unit (IFU) technology, which is able to explore the whole galaxy disk, has boosted galaxy metallicity studies. Studies based on CALIFA (Calar Alto Legacy Integral Field Area; Sánchez et al. 2012) confirm the deviations from pure linear metallicity profiles,

finding a flattening, or even a drop, in the inner region and/or an outer plateau at large radii in a fraction of galaxies (Sánchez et al. 2014; Sánchez-Menguiano et al. 2016, 2018). Belfiore et al. (2017) and Mingozzi et al. (2020) report that, in Mapping Nearby Galaxies at Apache Point Observatory (MaNGA; Bundy et al. 2015), metallicity profiles normalized by the effective radius tend to steepen with increasing stellar mass up to $10^{10.5}\,M_{\odot}$, in agreement with a small sample of Sydney-AAO Multi-object Integral field (SAMI; Croom et al. 2012) galaxies (Poetrodjojo et al. 2018), and then slightly flatten at higher masses. Azimuthal variations of the gas metallicity, driven by the spiral arms mixing and exchanging gas and metals with the inter-arm ISM, are observed in some Physics at High Angular resolution in Nearby GalaxieS (PHANGS) and TYPHOON galaxies (Ho et al. 2017, 2018; Kreckel et al. 2019, 2020).

Metallicity gradients stimulate interest in theoretical works that, on the one hand try to interpret the observations and explore the evolution of the gradient slope with redshift (Gibson et al. 2013; Ma et al. 2017; Hemler et al. 2021), and on the other hand aim at using the measured profiles to verify their recipes. For example, works based on semi-analytical models have tried to explain the diversity of gas metallicity gradients in galaxies, finding that mechanisms like radial motion, metal-poor and metal-rich gas accretion, turbulent transport, and outflow are involved in shaping the gas metallicity profiles and adding to the data scatter (Fu et al. 2013; Pezzulli & Fraternali 2016; Collacchioni et al. 2020; Sharda et al. 2021). Hydrodynamical simulations have exploited observed metallicity profiles to test the reliability of their simulated galaxies (Tissera et al. 2019; Valentini et al. 2019). To constrain the chemical evolution of galaxies it is also important to study the relation between metallicity gradients and galaxy properties. Lutz et al. (2021) report that the metallicity gradients positively correlate with the average stellar mass surface density and anti-correlate with the atomic gas mass.

In the literature, there is no general consensus on the role of environmental conditions in shaping the abundance gradients in disk galaxies. Exploiting MaNGA data, Schaefer et al. (2019) show that satellite galaxies with intermediate stellar masses are more metal-rich than centrals, but there is no obvious difference in the metallicity gradients. Lian et al. (2019) find that MaNGA low-mass satellites in denser environments tend to have flatter gas metallicity gradients and speculate on accretion of enriched material. In spite of the recent IFU surveys, the environmental dependence of the metallicity gradients is still an open question.

In this paper we study the radial distribution of ionized gas metallicity and stellar mass in the GAs Stripping Phenomena in galaxies with MUSE (GASP; Poggianti et al. 2017) sample, dividing galaxies according to their environment. GASP is an ESO Large Program carried out with the integral-field spectrograph MUSE that observed more than 100 galaxies with a spatial resolution of 1 kpc and a sky coverage of, on average, 8 effective radii. At the same time, we exploit a sample of MaNGA galaxies that allow us to strengthen the analysis on a more robust statistical basis. Our goal is to probe the difference due to the environment and find the processes that shape the metallicity profiles.

The paper is organized as follows. In Section 2, we explain the criteria adopted to select the galaxies from the GASP and MaNGA samples, whose data analysis are described in Section 3, together with the method adopted to derive the gas metallicity and the radial gradients. In Section 4, we present the main results of this paper, which are more widely discussed in Sections 5 and 6. Finally, Section 7 summarizes the conclusions of our study.

Throughout this work, we use a Λ cold dark matter cosmology with $\Omega_M = 0.3$, $\Omega_\Lambda = 0.7$, and $H_0 = 70\,\mathrm{km\,s^{-1}\,Mpc^{-1}}$, and a Chabrier (2003) initial mass function (IMF).

2. Galaxy Samples

2.1. GASP Sample

The GASP sample consists of 114 late-type galaxies in the redshift range $0.04 < z < 0.07$, observed in different environments (field, filaments, groups, and clusters). Observations were taken by the spectrograph MUSE (Bacon et al. 2010) at the Very Large Telescope (VLT), with wavelength coverage between 4800 and 9300 Å with a spectral resolution between $R = 1770$ and 3590. The field of view (FoV) is approximately $1' \times 1'$, with a spatial sampling of $0.''2\,\mathrm{pixel}^{-1}$ and a natural seeing of $\leqslant 1''$ (that corresponds to $\sim$1 kpc for galaxies in the sample). The large FoV provides a mean coverage of the sky of $8\,R_e$, which allows us to probe the entire ionized gas disk.

GASP targets are selected from *B*-band images of the WINGS (Fasano et al. 2006) and OMEGAWINGS (Gullieuszik et al. 2015) cluster surveys, and the PM2GC catalog (Calvi et al. 2011), with the intent of identifying gas anomalies in galaxies. Indeed, GASP collects galaxies undergoing a large variety of different physical processes, such as ram pressure stripping (RPS; e.g., Bellhouse et al. 2017, 2021; Gullieuszik et al. 2017, 2020; Poggianti et al. 2017, 2019; Moretti et al. 2018), interaction with the cosmic web (Vulcani et al. 2019a), and gas accretion (Vulcani et al. 2018a, 2018b), but undisturbed galaxies are also present (Vulcani et al. 2019b; Franchetto et al. 2020). However, focusing on single processes is beyond the scope of this work, as we are going to only explore the differences between galaxies in cluster and field galaxies.

From the initial sample, we exclude passive galaxies that do not show emission lines in the MUSE spectra (Vulcani et al. 2020a, 2021) and galaxies with truncated ionized gas disks (Fritz et al. 2017; Gullieuszik et al. 2020), whose metallicity gradient cannot be estimated. Moreover, we also remove galaxies undergoing a merging event (Vulcani et al. 2021), for which the radial metallicity profile might have been affected by the interaction. After this selection, we remain with a sample of 56 galaxies in clusters and 29 galaxies in less dense environments (field, filaments, and small groups) that we simply indicate as field galaxies.

2.2. MaNGA Sample

The MaNGA survey includes galaxies in the redshift range $0.01 < z < 0.15$, with a galaxy coverage fixed to $1.5\,R_e$, for the primary sample (2/3 of the MaNGA galaxies), and $2.5\,R_e$, for the secondary sample. Observations were carried out by the 2.5 m Sloan Digital Sky Survey (SDSS) telescope (Gunn et al. 2006) at the Apache Point Observatory. The FoV is simultaneously observed by 17 hexagonal fiber-bundle IFUs that vary in diameter, from 12″ to 32″ (Drory et al. 2015). Each fiber has a diameter of 2″ and feeds light into the two dual-channel BOSS spectrographs, which work in the spectral range between 3600 and 10300 Å with a resolution of $R \sim 1400$ at 4000 Å and $R \sim 2600$ at 9000 Å. For each target, three dithered

observations are combined to produce a data cube with square spaxels 0.″5 in size. The median point-spread function (PSF) of the MaNGA data cubes has a FWHM of 2.″5 (Bundy et al. 2015), corresponding to 0.5–6.5 kpc depending on the redshift.

The data used in this work are taken from the MaNGA DR15 catalog, which includes the outputs of the MaNGA data reduction pipeline (Law et al. 2016, and subsequent updates) for 4688 spatially resolved galaxies. First, we select galaxies with redshift $z < 0.08$ in order to better match the redshift range of the GASP sample. We take into account only galaxies classified as star-forming according to the classification scheme proposed in Belfiore et al. (2016), based on the diagnostic BPT diagram [O III]λ5007/Hβ versus [S II]$\lambda\lambda$6716,31/Hα (Baldwin et al. 1981; Kewley et al. 2001; Kauffmann et al. 2003). In addition, we exclude highly inclined systems (minor-major axis ratio $b/a < 0.4$). The selection leads to a sample of 1789 galaxies. We further classify the galaxies in subsamples based on the mass of the host halo reported in the catalog of groups and clusters of SDSS galaxies by Tempel et al. (2014). In order to match the host halo mass distribution of GASP galaxies, we identify 103 MaNGA galaxies in clusters with mass $M_{\rm h} > 10^{13.5}\,M_{\odot}$ and 1102 MaNGA galaxies in low-density environments ($M_{\rm h} < 10^{13}\,M_{\odot}$), while galaxies in the intermediate-mass halos are kept with no classification.

3. Data Analysis

3.1. GASP Data Analysis

A detailed explanation of methods employed in the analysis of the GASP data is available in Poggianti et al. (2017). Briefly, MUSE data cubes were reduced with the most updated version of the MUSE pipeline at the moment of observations (Bacon et al. 2010),[5] corrected for extinction due to our own Galaxy assuming the extinction law from Cardelli et al. (1989), and then, average filtered in the spatial direction with a 5×5 pixel kernel, corresponding to $1'' = 0.7$–1.3 kpc, depending on the galaxy redshift.

For each MUSE spaxel, we apply the spectrophotometric code SINOPSIS, which fits the spectrum with different sets of single stellar population models by S. Charlot and G. Bruzual to reproduce its main features and deliver the stellar-only component and the stellar mass (Fritz et al. 2017). Then, spectra are corrected for the underlying stellar absorption, and their emission-line fluxes and corresponding errors are measured using the IDL software KUBEVIZ (Fossati et al. 2016), which fits emission lines assuming a Gaussian profile. The correction for the extinction by dust internal to the galaxy is applied adopting the extinction curve of Cardelli et al. (1989) and assuming an intrinsic Balmer Hα/Hβ ratio of 2.86, appropriate for an electron density $n_{\rm e} = 100\,{\rm cm}^{-3}$ and electron temperature $T_e = 10^4$ K (Osterbrock 1989). Only spaxels with a signal-to-noise ratio (S/N) > 3 for all involved emission lines are considered.

In this work we focus on the values within the galaxy stellar body, whose boundary is defined as the region containing the spaxels whose underlying Hα continuum flux is $\sim 1\sigma$ above the background level (Gullieuszik et al. 2020). The external gas will be studied in a separated paper (A. Franchetto 2021, in preparation).

[5] http://www.eso.org/sci/software/pipelines/muse

For each galaxy, the inclination (i), the position angle (PA) of the disk, and the effective radius of the galaxy ($R_{\rm e}$) are estimated performing an isophotal analysis on the I-band images,[6] as done in Franchetto et al. (2020).

We use i and PA to deproject the coordinates of each spaxel onto the disk plane of the galaxy and to compute the galactocentric radius, fixing the galaxy center to the peak of the underlying Hα continuum flux. The correction for the disk inclination is not applied to galaxies with $i < 35°$ to avoid biases due to the uncertainties of the derived correction.

The total stellar mass of each galaxy is derived summing up the stellar mass values in all spaxels belonging to the galaxy disk, as in Vulcani et al. (2018c). We measure the stellar mass surface density by dividing the stellar mass in each spaxel by the pixel area expressed in kpc^2 units and corrected for the galaxy inclination.

For the cluster population, Gullieuszik et al. (2020) provide the projected clustercentric distances in units of cluster virial radius (R/R_{200}) and galaxy line-of-sight velocities with respect to cluster velocity dispersion ($|\Delta v|/\sigma_{\rm cl}$) that we use in Section 6.

3.2. MaNGA Data Analysis

The reduced MaNGA cubes are analyzed by the MaNGA data analysis pipeline v2.2.1 (Westfall et al. 2019; Belfiore et al. 2019a) that extracts the emission-line fluxes using a Gaussian fitting per line on stellar-continuum subtracted spectra. Stellar-continuum fitting is performed by the software PPXF (Cappellari & Emsellem 2004) that exploits a linear combination of the templates from the MILES stellar library (Falcón-Barroso et al. 2011). The line fluxes are corrected for the internal dust extinction adopting the Calzetti (1997) attenuation curve with $R_V = 4.05$ and assuming an intrinsic Balmer decrement Hα/Hβ = 2.86. Following Mingozzi et al. (2020), we exclude from further analysis the spaxels with S/N (Hα) < 15 and S/N < 1.5 for the other involved lines.

For each galaxy, the integrated stellar mass, the elliptical Petrosian effective radius $R_{\rm e}$[7], and the semi-axis ratio are taken from the NASA-Sloan catalog (NSA v1_0_1, Blanton et al. 2011). The deprojected distance of each spaxel is derived taking into account the galaxy inclination, computed from the semi-axis ratio and assuming an intrinsic oblateness of 0.13 (Giovanelli et al. 1994).

For 1310 galaxies, we can also derive the integrated gas fraction ($f_{\rm gas} = \log(M_{\rm H\,I}/M_{\odot})$), exploiting the atomic gas masses tabulated in the DR2 catalog of the H I-MaNGA survey (Masters et al. 2019; Stark et al. 2021).

We also take the orbital parameters (r/R_{200} and $|\Delta v|/\sigma_{\rm cl}$) of the cluster galaxies from the Tempel et al. (2014) catalog.

3.3. Gas-phase Metallicity Radial Gradients

In this section, we describe the method used to derive the metallicity of the ionized gas, here defined as oxygen abundance[8] 12 + log(O/H), its radial profile for each galaxy,

[6] The I-band images are derived by integrating the MUSE data cubes on the Cousin I-band response curve function.

[7] The elliptical Petrosian effective radius is the most robust measure of the photometric properties of MaNGA galaxies provided by the NSA catalog. Therefore, we use this quantity as an alternative to the effective radius adopted for GASP galaxies.

[8] We use the oxygen abundance as proxy of the metallicity of the gas (mass fraction of all metals), as it is the most abundant heavy element in the ISM.

and its gradient. We make the reader aware that for the GASP sample, which includes only 85 galaxies and extends to larger galactocentric radii, we carry out a more detailed analysis of the profiles, while for the 1789 MANGA galaxies we follow a simpler method, showing that the two methods are consistent for our purposes as discussed below. The methods described below are used both for GASP and MANGA, unless otherwise stated. First, we exclude the spaxels dominated by ionizing mechanisms other than star formation, using the diagnostic BPT diagram (Baldwin et al. 1981) [O III]λ5007/Hβ versus [N II]λ6583/Hα and the separation line of Kauffmann et al. (2003). Then, the gas-phase metallicity is estimated exploiting the strong emission lines of the ionized phase of the ISM. We adopt a modified version of the PYQZ code (Dopita et al. 2013; Vogt et al. 2015; F. Vogt 2017, private communication) that interpolates the observed flux ratios on the line-ratio model grid [O III]λ5007/[S II]$\lambda\lambda$6716, 6731 versus [N II]λ6383/[S II]$\lambda\lambda$6716, 6731 computed by MAPPINGSIV (Sutherland & Dopita 1993; Dopita et al. 2013), and delivers the metallicity and the ionization parameter of the emitting ionized gas. This version of PYQZ is tested in the range $7.39 \leqslant 12 + \log(\mathrm{O/H}) \leqslant 9.39$ and adopts the solar oxygen abundance of 8.69.

For GASP galaxies we also derive the error associated with the each metallicity value, as done in Franchetto et al. (2020). This error is calculated as the sum in quadrature of the error given by the propagation of the flux uncertainties and the systematic error that is introduced by the uncertainty of model grids that is usually of $\sim$0.1 dex (Kewley & Ellison 2008; Dopita et al. 2013; Blanc et al. 2015; Mingozzi et al. 2020).

Assuming that galactic disks are axis-symmetric, for each galaxy, we compute the gradient of the azimuthally average metallicity profile, derived by radial binning. The binning allows us to minimize the effects of possible azimuthal variations in the metallicity distribution, and better highlights the radial gradient. All profiles are scaled by the R_e of the galaxy to facilitate a fair comparison between galaxies of different sizes. Considering the adopted normalizing scale length, all gradients presented in this work are in units of dex R_e^{-1}; therefore, we stress that any consideration on this quantity refers to this chosen notation.

For GASP galaxies we use radial bins of 0.1 R_e, while for MANGA, which has a lower spatial resolution, we adopt bins of 0.2 R_e. In each radial bin, we compute the mean metallicity and its standard deviation. For GASP galaxies, we also derive the error given by the propagation rules applied to the metallicity uncertainties, which we sum in quadrature with the standard deviation.

The metallicity profiles are not always described by a simple linear behavior, as they can also show deviations, like breaks in the slope either at small and large radii (Sánchez et al. 2014; Bresolin 2015; Sánchez-Menguiano et al. 2016). Typically, in the literature the gradients of the metallicity profiles are computed between 0.5 and 2 R_e in order to avoid biases due to the presence of these features. However, the exact positions of the breaks are variable and fixing the radial range of the gradient computation could partially affect the results, especially when the sample is small.

Since we can probe the entire ionized gas disk of GASP galaxies and we more finely binned their metallicity profiles than MaNGA ones, for GASP galaxies we compute the metallicity gradients with a more sophisticated method, with no assumptions on the presence of the inner and/or outer deviating behaviors, following the procedure performed by Sánchez-Menguiano et al. (2018). In detail, we fit the whole profile with three different parameter functions: (1) a "single-linear" profile, (2) a broken linear profile ("double-linear") with a change in slope, and (3) doubly broken linear profile ("triple-linear") with both an inner and an outer break. The mathematical functions are designed as follows:

1. The "single-linear" profile is given by
$$12 + \log(\mathrm{O/H})(r) = \alpha_{\mathrm{O/H}}(r - 1) + Z_{R_e} \quad (1)$$
where the radial coordinate r is expressed in units of R_e and $\alpha_{\mathrm{O/H}}$ is the slope of the metallicity profile.
2. The "double-linear" profile consists of a broken linear function split at R_b; at $r < R_b$ the function is
$$12 + \log(\mathrm{O/H})(r) = \alpha_{\mathrm{in}}(r - 1) + Z_{R_e}, \quad (2)$$
while at $r > R_b$ it is
$$12 + \log(\mathrm{O/H})(r) = \alpha_{\mathrm{out}}(r - R_b) + \alpha_{\mathrm{in}}(R_b - 1) + Z_{R_e}. \quad (3)$$
If the deviation from the main gradient is located at $r > R_b$, we define $\alpha_{\mathrm{in}} \equiv \alpha_{\mathrm{O/H}}$; if, instead, it occurs in the inner part, $\alpha_{\mathrm{out}} \equiv \alpha_{\mathrm{O/H}}$.
3. The "triple-linear" profile is a doubly broken linear function with both an inner flattening at R_{in} and an outer plateau beyond R_{out}; this function is characterized by three segments, where the middle one, at $R_{\mathrm{in}} < r < R_{\mathrm{out}}$, is given by Equation (1), while the segment at $r < R_{\mathrm{in}}$ is
$$12 + \log(\mathrm{O/H})(r) = \alpha_{\mathrm{in}}(r - R_{\mathrm{in}}) + \alpha_{\mathrm{O/H}}(R_{\mathrm{in}} - 1) + Z_{R_e} \quad (4)$$
and the part at $r > R_{\mathrm{out}}$ is
$$12 + \log(\mathrm{O/H})(r) = \alpha_{\mathrm{out}}(r - R_{\mathrm{out}}) + \alpha_{\mathrm{O/H}}(R_{\mathrm{out}} - 1) + Z_{R_e}. \quad (5)$$

The slopes ($\alpha_{\mathrm{O/H}}$, α_{in}, and α_{out}) are in units of dex R_e^{-1}, all radii are expressed in units of R_e, and $Z_{R_e} \equiv 12 + \log(\mathrm{O/H})(R_e)$.

A posteriori, we choose only the functional shape that best describes the observed metallicity profile by applying the corrected Akaike Information Criterion[9] (AICc; Akaike 1974; Hurvich & Tsai 1989) to the three best fits. The AICc evaluates the goodness of each fit penalizing, at the same time, the loss of degrees of freedom. The lowest AICc value indicates the best function.

The fitting procedure is carried out adopting the Python module EMCEE (Foreman-Mackey et al. 2013) that performs a Markov Chain Monte Carlo (MCMC) sampling of the multi-dimensional parameter space. The best-fit parameters are derived maximizing the Gaussian likelihood function that takes into account the uncertainties of the data points and imposing uniform priors in the following ranges: $\alpha_{\mathrm{O/H}}$, α_{in}, and $\alpha_{\mathrm{out}} \in [-1.0, 0.5]$, $Z_{R_e} \in [7.6, 9.3]$, and R_b, R_{in}, and $R_{\mathrm{out}} \in [\min(r), \max(r)]$, where $\min(r)$ and $\max(r)$ refer to the extremities of the metallicity profiles. In addition, we impose that $R_{\mathrm{in}} < R_{\mathrm{out}}$. From the marginalized distributions of each sampled parameter, we compute the median and the semi-range between the 16th and 84th percentiles. In Appendix B, we

[9] With respect to the Akaike Information Criterion (AIC; Akaike 1974), the AICc introduces a second-order penalty term that better performs in small samples.

report the best-fit $\alpha_{O/H}$ values and the corresponding uncertainties for each galaxy in our GASP sample. In this work, we do not use the other best-fit parameters (R_b, R_{in}, R_{out}, α_{in}, and α_{out}), but they are tabulated in Appendix C.

Figure 1 shows the metallicity maps for four GASP galaxies and the corresponding radial profiles, in order to provide illustrative examples of the variety of metallicity profiles and their best fits. The metallicity profile of A3266_B_0257 is represented by a "single-linear" function. P17945 and JO5 show "double-linear" profiles, where the former is characterized by an outer plateau and the latter by an inner flattening. The metallicity profile of P21734 is a clear example of "triple-linear" profile.

Note that the ISM contains a large amount of diffuse ionized gas (DIG, e.g., Haffner et al. 2009). This warm component is more extended than star-forming associations and its ionizing source is still unclear. In some cases, discrepancies between metallicities derived from spectra of H II regions and spectra dominated by DIG are reported (Zhang et al. 2017; Poetrodjojo et al. 2019; Vale Asari et al. 2019). Tomičić et al. (2021a) estimated the fraction of DIG for the galaxies in GASP, exploiting the Hα surface brightness and the [S II]/Hα line ratio measured in each spaxel, and found that the DIG emission contributes between 20% and 90% of the flux. In order to test the robustness of our metallicity gradients against the DIG contamination, we checked that the azimuthally averaged radial profiles of the metallicity do not significantly change if we repeat the computation penalizing the spaxels dominated by DIG emission (the mean variation of the metallicity gradients is within 0.02 dex R_e^{-1}). In addition, Tomičić et al. (2021b) statistically look for a difference in metallicity between dense gas and DIG within same radial bins, and find that the difference is lower than the scatter within bins and uncertainties in metallicities.

The method used to calculate the metallicity gradients for GASP galaxies is not suitable for the galaxies in the MaNGA sample, as MaNGA observations have a smaller FoV and lower spatial resolution. Therefore, we fit the metallicity profiles of MaNGA galaxies using Equation (1) in the radial range 0.5–2 R_e. To understand how much the choice of the parameterization affects the results, for GASP galaxies we also compute gradients using the same approach adopted for MaNGA. In Figure 2, we compare the gradients obtained by this method with those given by the previous one. There is a clear correlation, though fitting the metallicity profiles with a linear function in a fixed radial range provides, on average, slightly shallower gradients by 0.027 ± 0.055 dex R_e^{-1}.

3.4. Stellar Surface Mass Density Gradients

Metallicity well correlates with the stellar mass (e.g., MZR, Tremonti et al. 2004; Franchetto et al. 2020), and in our analysis we aim at investigating if this connection persists also between the radial gradients of these two quantities.

For GASP, we compute $\Sigma_\star$ gradients from the stellar mass surface density $\Sigma_\star$ from SINOPSIS. In principle, we should use the integral of the SFR over the whole galaxy history (all of the stellar mass ever formed), which should be more closely related to the metals produced. However, this quantity requires a detailed star formation history reconstruction that is not available for MaNGA (see below), so we just use the current stellar mass density instead. We have checked that the two quantities give consistent results.

For MaNGA, we exploit the maps of stellar mass surface density provided in the MaNGA Pipe3D Value Added Catalog of SDSS DR15 (Sánchez et al. 2016). The stellar population properties of MaNGA galaxies are derived using the fitting code FIT3D (Sánchez et al. 2006) and the single stellar populations template library of Cid Fernandes et al. (2013). We use these $\Sigma_\star$ maps with a correction factor of 0.24 dex to scale the values down from a Salpeter to a Chabrier IMF.

We derive the azimuthally averaged radial profiles of $\Sigma_\star$ (expressed in a logarithmic scale of $M_\odot$ kpc^{-2} units), applying the same radial binning adopted for the metallicity (Section 3.3). The $\Sigma_\star$ profiles are typically linearly decreasing up to, on average, 2.5 R_e, with a possible outer plateau (an example of a $\Sigma_\star$ profile is shown in Appendix A). Therefore, these profiles do not manifest the intrinsic complexity observed in the metallicity profiles, and we estimate the gradient of the stellar mass surface density ($\alpha_{M\star}$) by fitting a linear function between 0.5 and 2.0 R_e. This also allows us to avoid possible biases due to the presence of massive bulges, which usually have steeper mass profiles than the disks (González Delgado et al. 2014). We apply an MCMC fitting using the Python module EMCEE and imposing the following uniform priors on the free parameters: $\alpha_{M\star} \in [-1.5, 1.0]$ and $\Sigma_{\star Re} \in [6, 10]$, where $\Sigma_{\star Re}$ is the stellar mass surface density at R_e. All $\alpha_{M\star}$ values of GASP galaxies are reported in Table 1.

4. Results

4.1. The Distribution of the Metallicity Gradients

One of the goals of this paper is to investigate the dependence of the gas metallicity gradients on the galaxy environment. Figure 3 illustrates the distribution of the metallicity gradients of the GASP (on the left) and MaNGA (on the right) samples as a function of stellar mass. We note that our intent is to explore the same trends in both samples and all the comparisons will be exclusively qualitative.

First, we focus on the left panel corresponding to the GASP sample. Before explaining in detail the results, we list the main observed features:

1. All metallicity gradients are negative, except for two low-mass galaxies that are positive but close to zero.
2. No low-mass galaxy exhibits a very steep metallicity gradient, but gradients tend to become steeper with increasing stellar mass up to $M_\star \sim 10^{10.3} M_\odot$.
3. The scatter of the metallicity gradient−mass relation increases for the intermediate masses.
4. The massive galaxies ($M_\star > 10^{11} M_\odot$) show very flat metallicity profiles ($\alpha_{O/H} > -0.05$ dex R_e^{-1}).
5. At $M_\star < 10^{10.3} M_\odot$, cluster galaxies have, on average, shallower metallicity profiles than field galaxies of similar mass.

Negative metallicity gradients trivially mean that the ISM in the central regions of the galaxies has a higher metallicity than the outer gas, as expected according to the inside-out formation of disk galaxies (Searle 1971). We note that the bottom left corner of the diagram shown in Figure 3, corresponding to the region at low masses and lower metallicity gradients, contains no galaxies. This is a sort of "*forbidden region*," suggesting that low-mass galaxies cannot develop very steep metallicity profiles. The indicative limit of this region is given by the

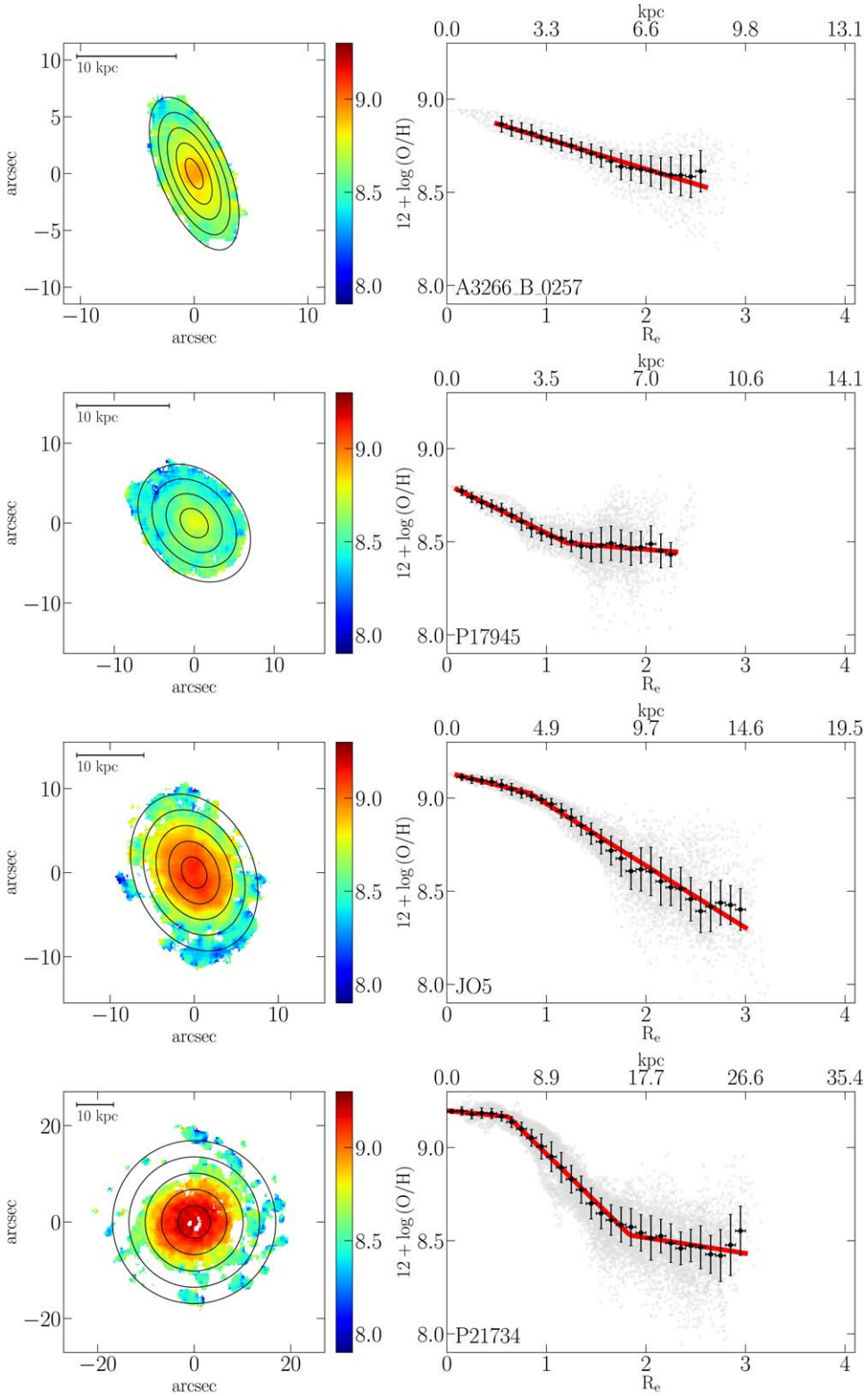

Figure 1. Left panels: gas metallicity maps for the galaxy A3266_B_0257, P17945, JO5, and P21734. Concentric ellipses indicate the radial distance from the galaxy center, with incremental steps of 0.5 R_e. We just remark that the PSF $\leqslant 1''$. Right panels: gas metallicity profiles of the respective galaxies. Gray small points correspond to the spaxel gas metallicities. Black dots show the azimuthally averaged radial profile of the metallicity and the associated uncertainties. Horizontal error bars indicate the size of the radial bins. Red curves are the best fits. The complete figure set of 85 images (one for each galaxy) is available in the online journal. The azimuthally average gas metallicity profiles of each GASP galaxy are available as the Data behind the Figure.

(The data used to create this figure are available.)

(The complete figure set (85 images) is available.)

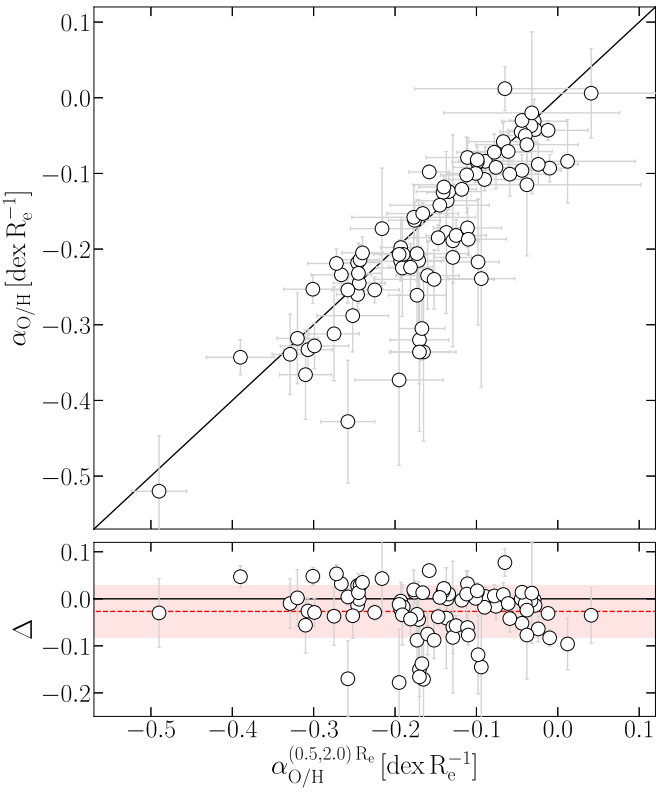

Figure 2. Comparison between the metallicity gradients estimated fitting the whole profile with a broken linear function and those derived by the linear fit between 0.5 and 2.0 R_e for the GASP sample. The black line indicates the 1:1 relation. Lower panel: distribution of differences between the two quantities. Red dashed line and faded area show the average offset and the standard deviation, respectively.

equation

$$\alpha_{O/H} = -0.199\,[\log(M_\star/M_\odot) - 10] - 0.432. \quad (6)$$

This latter formula was empirically obtained by a linear fitting of the minimum value of metallicity gradients in four stellar mass uniform bins between 10^9 and $10^{11}\,M_\odot$, then shifted downward by 0.05 dex to keep all galaxies above the line. This line is not a strict limit, but it just delimits empirically a region where galaxies are not typically found.

It appears clear that field and cluster galaxies of the GASP sample have different stellar mass distributions. To minimize possible biases, we divide the GASP sample in two stellar mass ranges, using a separation mass of $\log(M_\star/M_\odot) = 10.3$ as a reference. We highlight that a different choice included between $\log(M_\star/M_\odot) = 10$ and 10.5 does not significantly impact our conclusions. For galaxies with $M_\star < 10^{10.3}\,M_\odot$, we observe an anti-correlation between metallicity gradient and stellar mass (Pearson correlation coefficient PCC $= -0.55$; p-value $= 10^{-5}$). Field galaxies are, on average, 0.09 dex closer to the margin of the forbidden region than cluster galaxies, while cluster galaxies manifest a larger scatter of metallicity gradients spreading above the field population. The Kolmogorov–Smirnov (KS) test confirms with a high probability that the distributions of metallicity gradients of the two populations are different (p-value $= 0.002$). For $M_\star > 10^{10.3}\,M_\odot$, we find a moderate positive correlation with the stellar mass (PCC $= 0.38$; p-value $= 0.03$). Both field and cluster galaxies span a wide range of metallicity gradients. At the highest stellar masses, above $\sim 10^{11}\,M_\odot$, all galaxies exhibit shallow metallicity profiles ($\alpha_{O/H} > -0.05$ dex R_e^{-1}).

Now, we examine in the right panel of Figure 3 the results based on the MaNGA sample. This large sample allows us to increase the statistics and verify the results obtained from the GASP sample. Overall, the distribution of metallicity gradients as a function of the stellar mass is qualitatively in agreement with that of the GASP sample. The main findings are:

1. We find an anti-correlation between stellar masses and metallicity gradients up to $10^{10.3}\,M_\odot$, and a correlation at higher stellar masses. However, both relations are weaker than those found for the GASP sample.
2. At intermediate masses (around $10^{10.3}\,M_\odot$), we observe a large spread (more than 0.3 dex) of metallicity gradient values.
3. Cluster galaxies have, on average, flatter metallicity gradients than field galaxies and, in particular, the population of cluster galaxies has fewer steep metallicity profiles than the population of field galaxies at a given stellar mass.

The distribution of the metallicity gradients as a function of stellar mass is similar of that of the GASP sample. At the lowest and the highest masses, galaxies have shallow profiles, while moving toward intermediate masses, galaxies can exhibit also steep profiles. No galaxy with a steep gas metallicity profile is found at the lowest masses (i.e., in the forbidden region), but nor are any found at the highest masses, suggesting the presence of a further forbidden region at these masses.

The PCC attests to the presence of a mild anti-correlation at $M_\star < 10^{10.3}\,M_\odot$ (PCC $= -0.27$; p-value $= 10^{-18}$), and a weak correlation at $M_\star > 10^{10.3}\,M_\odot$ (PCC $= 0.25$; p-value $= 10^{-10}$). The weakness of these trends with mass resides in the large scatter of gradient values that fill all of the area above the forbidden regions. In particular, the largest scatter is observed around $M_\star = 10^{10.3}\,M_\odot$, where 90% of galaxies with this stellar mass span more than 0.3 dex. A small fraction of galaxies (3%) shows inverted profiles (i.e., positive gradients), which could be ascribed to a contamination of merging systems (Rich et al. 2012; Grossi et al. 2020).

To study the dependence of the metallicity gradients on the stellar mass, we divide the MaNGA sample in five stellar mass bins delimited by the values $\log(M_\star/M_\odot) =$ 8.9, 9.5, 9.9, 10.3, 10.7, 11.3,[10] and estimate the median metallicity gradient in each bin. First of all, we consider all 1789 MaNGA galaxies regardless of their environment, finding again a weak relation between metallicity gradients and stellar masses. On average, the metallicity profiles become slightly steeper up to intermediate masses ($\sim 10^{10.3}\,M_\odot$) and then flatten toward higher mass values. To provide a qualitative comparison between the GASP and MaNGA samples, we also estimate the median metallicity gradients of the GASP sample in the same stellar mass bins, finding a similar relation, albeit the values are different.

Coming back to the MaNGA sample, we now contrast the field and the cluster populations to highlight possible differences due to the environment. For four out of five stellar mass bins, median gradients of cluster galaxies are $\sim$0.03 dex shallower than those of field galaxies, although the KS test is not conclusive to verify a statistical difference between the two

[10] The first and last bins are larger to increase the statistics.

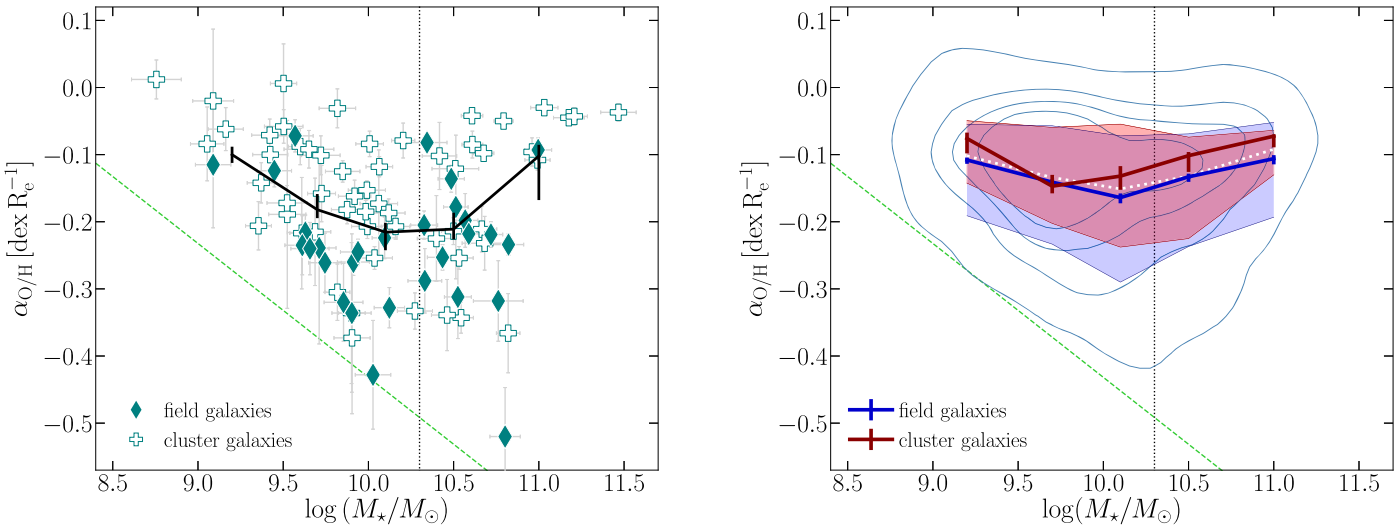

Figure 3. Gas metallicity gradient as a function of galaxy stellar mass. Left: distribution of 29 field and 56 cluster GASP galaxies, depicted with filled elongated diamonds and empty crosses, respectively. Black line indicates the median in five stellar mass bins (see the text). Right: contours enclosing the distribution of 35%, 55%, 75%, and 95% of MaNGA galaxies. Dotted white, solid blue, and solid red curves refer to the medians of the whole MaNGA sample, only field galaxies, and only cluster galaxies, respectively, in five stellar mass bins (see the text). The blue and red faded area indicate the range between the 16th and 84th percentiles. The vertical error bars are the 16th and 84th percentile range divided by $\sqrt{N}$, where N the number of galaxies in the stellar mass bin. In both panels, the vertical dotted line indicates the stellar mass at $10^{10.3}$ $M_\odot$ and the dashed green line represents the limit of the forbidden region (Equation (6)).

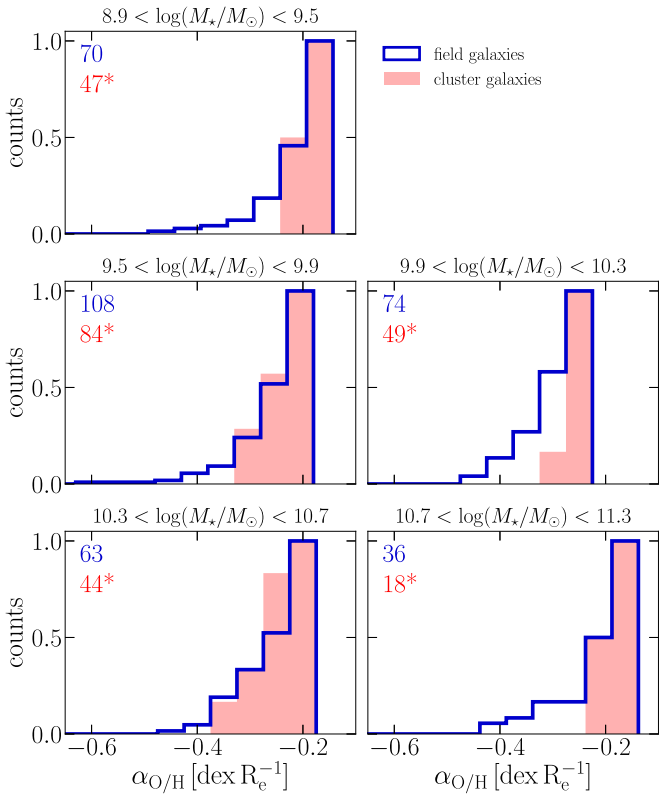

Figure 4. Cumulative distributions in five stellar mass bins of the gradients of the MaNGA metallicity profiles of field (blue) and cluster (red) galaxies that are steeper than the 33th percentile, in each bin, of the metallicity gradients of field galaxies. The numbers in the top-left corner of each panel indicate the number of field (blue) and cluster (red) galaxies within the corresponding stellar mass bin. The asterisk indicates that the number is normalized to take into account the fact that cluster galaxies are fewer than field galaxies by an order of magnitude.

populations. We find that, in each stellar mass bin, the vast majority of cluster and field galaxies occupy the same region of the $\alpha_{O/H}-\log(M_\star/M_\odot)$ plane, but field galaxies show a tail of galaxies with low metallicity gradients (lower by ∼0.05) that is absent in clusters.

In order to examine in detail this difference we select, in each stellar mass bin, those field and cluster galaxies whose metallicity profiles are steeper than the 33th percentile of the metallicity gradients of field galaxies and we show the cumulative distributions of their metallicity gradients in Figure 4. In each stellar mass bin, there is a number of field galaxies with steeper metallicity profiles than cluster galaxies. We exclude the possibility that this difference is due to either the smaller number of cluster galaxies relative to the field population or a statistical fluctuation in the number of galaxies. Indeed, if we assume that the number of galaxies is affected by a Poissonian statistical error and take into account that the cluster galaxies are one order of magnitude fewer than the field population, we find that, in each stellar mass bin, the amount of field galaxies with steep metallicity profiles (i.e., metallicity gradients lower than the 33th percentile) is greater than 2σ than the number of cluster galaxies. Therefore, we can conclude that cluster members do not show steep metallicity profiles as field galaxies do.

To summarize, GASP and MaNGA galaxies show a characteristic distribution of metallicity gradients as a function of the stellar mass, where low-mass and high-mass galaxies present shallow metallicity profiles that become steeper moving toward intermediate masses. The cluster population has, on average, flatter profiles than field galaxies at similar stellar masses.

4.2. The Distribution of the Stellar Surface Mass Density Gradients

Under the assumption that the effect of stellar migration (Grand et al. 2015; Debattista et al. 2017) and tidal interaction are negligible, the stellar mass gradient provides a proxy for the mass assembly history of a galaxy as it indicates the amount of stars at each radius. Therefore, this quantity can provide a point

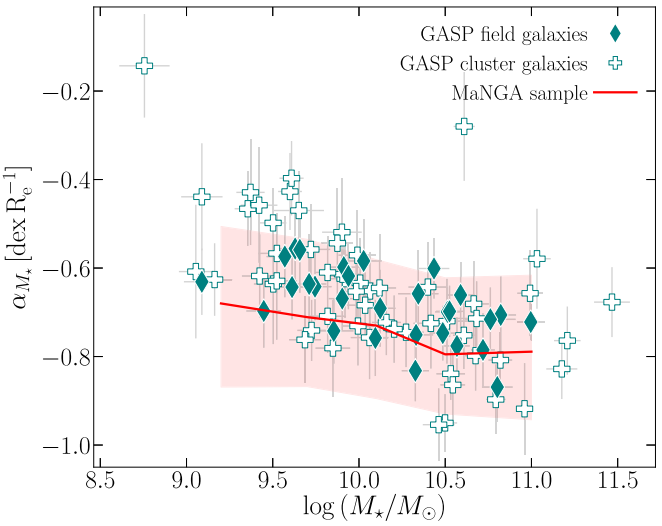

Figure 5. Distribution of stellar mass gradients of GASP galaxies as a function of stellar mass. Empty crosses and filled elongated diamonds refer to cluster and field galaxies, respectively. The red line and the faded area indicate the median trend and the range between the 16th and 84th percentiles of MaNGA galaxies.

of view complementary to the metallicity gradients for studying the evolution of galaxies.

Figure 5 illustrates the stellar mass surface density gradient (stellar mass gradient for brevity) as a function of stellar mass for field and cluster galaxies in the GASP sample. As expected, all stellar mass gradients are negative, indicating that the central regions are denser than the outer ones. In addition, we observe that:

1. The stellar mass gradients are clearly anti-correlated with the galaxy stellar mass[11] (PCC $= -0.59$; p- value $= 10^{-9}$), as already observed in González Delgado et al. (2014).
2. Field and clusters galaxies are placed along the same sequence.

The lack of offset between field and cluster galaxies suggests that the radial distribution of the assembly history does not depend on the environment and that the stellar mass profile is probably mainly dominated by stars formed before the galaxy fell in the cluster. In Figure 5 we also show the median trend of MaNGA galaxies along with the 16th and 84th percentiles, computed in the five stellar mass bins adopted in Figure 3. Although the $\Sigma_\star$ profiles of MaNGA galaxies are, on average, slightly steeper than the GASP ones, we qualitatively find a similar trend. We stress that the $\Sigma_\star$ gradients of the two samples cannot be directly compared because the procedures adopted by the two surveys to derive the stellar masses present substantial differences; for instance, the different sets of single stellar population models used to fit the spectra. Moreover, in contrast to GASP data, MaNGA data require a spatial binning to reach a S/N > 50.

5. Mass Dependence of Metallicity Gradients

In the previous section, we showed that the gas metallicity gradients of both GASP and MaNGA samples are characterized by some remarkable properties: (1) all gradients are consistent with negative values, i.e., the inner regions are more metal-rich than the outskirts; (2) the metallicity profiles become steeper with increasing stellar mass up to $10^{10.3}\,M_\odot$, while at higher masses the metallicity profiles become shallower; (3) at intermediate stellar masses ($\sim 10^{10.3}\,M_\odot$), the scatter significantly increases; (4) stellar mass profiles steepen monotonically with the stellar mass. In this section, we want to understand the physical reasons that are shaping the metallicity profiles: which scenario may explain the steepening of the metallicity profiles as the stellar mass increases up to intermediate masses, also in light of the variation of the stellar mass gradients with galaxy mass? Why do massive galaxies tend to have shallow profiles?

The scenario in which metallicity gradients depend on the stellar mass is qualitatively in agreement with other works in the literature based on MaNGA, SAMI, and CALIFA data, adopting different metallicity calibrators (Pérez-Montero et al. 2016; Belfiore et al. 2017; Poetrodjojo et al. 2018; Mingozzi et al. 2020). Some authors, using the CALIFA sample, do not detect any mass dependence and, instead, point to a universal metallicity gradient (Sánchez et al. 2014; Sánchez-Menguiano et al. 2016). However, from the values of metallicity gradients and stellar mass published in Sánchez-Menguiano et al. (2016), we find a correlation for $M_\star > 10^{10.3}\,M_\odot$ (PCC $= 0.35$; p-value $= 0.001$), consistent with our results.

5.1. Star Formation as Primary Regulator of Metallicity Profiles

The inside-out formation implies that the central regions of a disk galaxy rapidly grow, becoming more metal-rich and more massive in stars per unit area than the peripheral part of the galaxy, and producing radial negative gradients in stellar mass and metallicity (Larson 1976; Prantzos & Boissier 2000). Keeping this in mind, here we want to investigate the physical reason behind the mass dependence of the metallicity gradients, and we start considering the in situ chemical enrichment due to star formation along the galaxy disk. If we assume that there is no radial motion of gas, the increase in metallicity is directly proportional to the number of stars formed at each radius. The natural expectation is that the metallicity gradients will correlate with stellar mass gradients: the larger amount of stars formed at a given location in the galaxy, the higher the metallicity we should observe. We can test this prediction using GASP galaxies and in the top panel of Figure 6 we compare the two gradients. Despite the large scatter, we find a mild correlation (PCC $= 0.28$; p-value $= 0.009$). In addition, we observe that, while flat metallicity profiles can be found in the presence of both steep and flat stellar mass profiles, the steep metallicity profiles can be found only in galaxies with steep stellar mass profiles. In the bottom panel, we propose again the distribution of metallicity gradients as a function of stellar mass of the GASP galaxies. To separate galaxies with a similar stellar mass, but a different metallicity gradient, for each galaxy we compute the distance $\Delta\alpha_{O/H}$ from the forbidden region (Equation (6) and dashed green line in the figure) and color code the galaxies in both panels of Figure 6 according to this quantity. The closest galaxies to the forbidden region are depicted by yellow symbols; the steepening of their metallicity profiles goes at the same pace as the stellar mass profiles steepen, and indeed we find a strong correlation (PCC $= 0.60$; p-value $= 0.0005$). By contrast, the massive galaxies color coded by dark green, have flat metallicity

[11] The galaxy with a shallow stellar mass profile and a high stellar mass is JO171: an example of Hoag-type galaxy (Moretti et al. 2018).

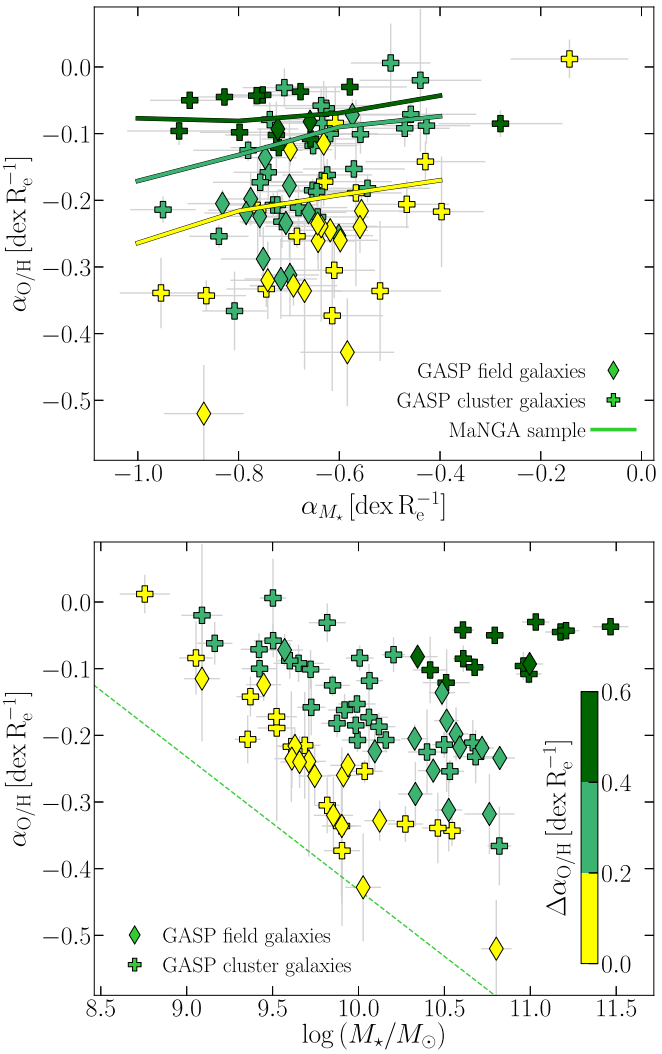

Figure 6. Distribution of metallicity gradients as a function of the stellar mass gradient (upper panel) and the stellar mass (lower panel) for GASP galaxies. Elongated diamonds and crosses refer to field and cluster galaxies, respectively, color coded by the distance $\Delta\alpha_{O/H}$ from the forbidden region (Equation (6) and dashed green line in the lower panel). For a qualitative comparison, the three lines in the upper panel refer to the median trends of MaNGA galaxies, with the same color code used for GASP galaxies.

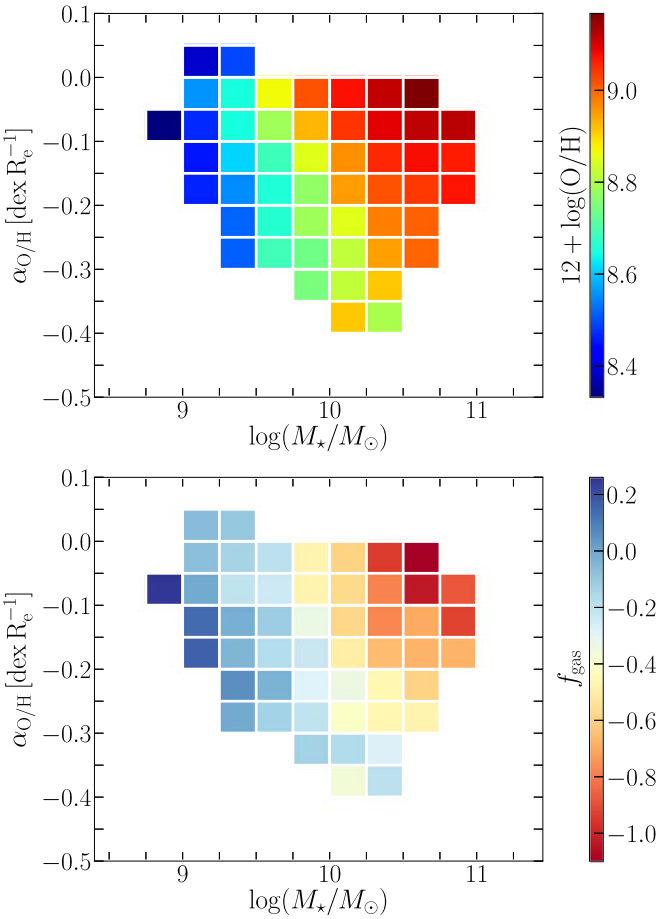

Figure 7. Distribution of metallicity gradients of the MaNGA sample as a function of the stellar mass, color coded by the mean metallicity at the effective radius (upper panel) and the mean gas fraction (lower panel). Galaxies are binned in stellar mass (size of 0.25 dex) and metallicity gradient (size of 0.05 dex R_e^{-1}).

profiles ($\langle\alpha_{O/H}\rangle = -0.07$ dex R_e^{-1}), although their stellar mass profiles are, on average, steep ($\langle\alpha_{M\star}\rangle = -0.71$ dex R_e^{-1}).

In order to verify this behavior for MaNGA galaxies, we probe the distribution of their gas metallicity gradients against the stellar mass gradients, and we show in the top panel of Figure 6 the median values computed in four equally spaced stellar mass gradients bins dividing the galaxies according to their $\Delta\alpha_{O/H}$ values. Although we restate that the two samples are not quantitatively comparable, overall, we find the same trends observed in the GASP sample, even if the MaNGA sample presents a larger scatter and the correlations are milder, but significant (on average PCC = 0.20; p-value $\ll 0.05$).

The emerging picture suggests that the in situ star formation, and the subsequent metal enrichment, play a primary role in steepening the profiles of stellar mass and, consequently, metallicity in disk galaxies. This produces, first, the correlation between stellar mass gradients and metallicity gradients and, second, the anti-correlation between gradients and stellar masses. This appears to be the dominant mechanism regulating the metallicity profiles up to intermediate stellar masses. However, the metallicity of the gas is not only determined by the enrichment due to the star formation, but it is also connected to other parameters that might contribute to flatten the metallicity profiles and can be dominant in clusters and at high stellar masses, where we observe the most significant deviations.

5.2. Dependence on the Gas Fraction

Overall, our results show a steepening (up to ~ -0.4 dex R_e^{-1}) of the metallicity profiles with increasing stellar mass up to $\sim 10^{10.3}\,M_\odot$. However, many galaxies present shallow (< -0.1 dex R_e^{-1}) profiles (especially in clusters) at every mass, and an overall flattening of all profiles toward high masses.

Belfiore et al. (2017) find that galaxies with a lower specific SFR have flatter metallicity profiles and suggest that the metallicity flattening in the central regions of massive galaxies could be due to the general behavior of evolved galaxies to reach an equilibrium abundance at late times, corresponding to low gas fractions. The connection between metallicity and the gas content is well established: Brown et al. (2018) demonstrate that at a given stellar mass, the metallicity

decreases as the neutral gas mass increases (see also Stark et al. 2021). Moreover, Ascasibar et al. (2015) observe that the relation between metallicity and gas fraction also holds at local (1 kpc) scales. Carton et al. (2015) study 23 H I-rich galaxies, finding that they have steeper metallicity profiles than galaxies with a normal H I gas content and similar mass. Lutz et al. (2021) show that metallicity gradients are anti-correlated with the atomic gas mass fraction. Boardman et al. (2021) report that at a given stellar mass MaNGA galaxies with steeper metallicity profiles are larger in size, and Sánchez Almeida & Dalla Vecchia (2018) argue that galaxies bigger in size have experienced late gas accretion and have lower metallicities than more compact counterparts. Collacchioni et al. (2020), using cosmological hydrodynamical simulations, conclude that galaxies with high rates of gas accretion have steep metallicity profiles in the inner regions. Analytic models show that radial motions induced by gas accretion steepen the profiles of chemical abundances (Pezzulli & Fraternali 2016).

In light of the connection between metallicity and gas content, we investigate the dependence of the metallicity gradients on the gas fraction. To this aim, we exploit the MaNGA sample, for which we have the information on the H I content. In Figure 7, we show the metallicity gradients versus stellar mass, where galaxies are binned in stellar mass (bins of 0.25 dex) and metallicity gradient (bins of 0.05 dex R_e^{-1}). Each bin contains at least five galaxies, for which we calculate the mean metallicity at R_e (upper panel) and the mean gas fraction (lower panel). Moving from left to right, as the stellar mass increases the metallicity increases and the gas fraction decreases. In addition, moving from the bottom to the top, at a given stellar mass the metallicity profiles tend to become flatter as the metallicity increases and the gas fraction decreases. Galaxies with a high gas content ($f_{\rm gas} > -0.2$) show a tight anti-correlation between stellar mass and metallicity gradient, supporting the steepening of the metallicity profiles with stellar mass for galaxies whose star formation is in equilibrium with the available amount of gas.

Given the clear presence of a further dependence of the gas metallicity gradients on a third parameter (gas fraction or gas metallicity at R_e), in addition to the stellar mass, we fit a three-dimensional surface on the three variables. First, for the two alternative parameters, we binned galaxies in stellar mass (bins of 0.25 dex) and gas fraction (bins of 0.2 dex), and in stellar mass and gas metallicity (bins of 0.1 dex), and we derived the mean gas metallicity gradient in each bin (bins with less than five galaxies are excluded). Then, we fit the mean values with a second-order polynomial surface deriving the relations:

$$\alpha_{\rm O/H} = -0.46x + 0.02x^2 + 0.83y - 0.04y^2 - 0.09xy + 2.61; \quad (7)$$

$$\alpha_{\rm O/H} = -0.76x + 0.003x^2 - 6.10z + 0.32z^2 + 0.07xz + 29.89, \quad (8)$$

where $x = \log(M_\star/M_\odot)$, $y = f_{\rm gas}$, and $z = 12 + \log({\rm O/H})$ at R_e. The root mean square of the deviations (RMSD) for Equation (7) are 0.021 and 0.084 considering the mean metallicity gradients and all MaNGA galaxies, respectively; while, for Equation (8), RMSD = 0.034 and 0.078. Both proposed relations are able to follow the shape of the data and completely remove the dependencies of the residuals. The two surfaces are shown in Appendix D.

To conclude, our result provides the evidence that, as galaxies consume or lose their gas reservoir, the metallicity increases, in particular at large radii, causing the flattening of the metallicity profile.

5.3. Brief Summary

Thanks to our analysis of the metallicity gradients as a function of the stellar mass gradients and the galaxy gas fraction, we are in the position to propose an explanation for the variety of metallicity gradients found in galaxies of different masses:

1. Low-mass galaxies: although these systems have a large gas fraction, they are not able to produce steep stellar mass profiles, thus their metallicity profiles tend to remain flatter than more massive galaxies.
2. Intermediate-mass galaxies: for these galaxies the radial variation (from the center to the outskirts) of star formation is larger, producing steep stellar mass profiles, but they can present a large variety of metallicity gradients. Indeed, as long as the consumption of the gas due to star formation is balanced by a new gas supply, the metallicity profiles can steepen in accordance with the stellar mass gradients; instead, if the gas fraction decreases, the metallicity profiles tend to flatten.
3. High-mass galaxies: although these systems have very steep stellar mass profiles, they are in an advanced stage of their evolution, where most of their gas content was consumed and the metallicities are high at all radii, entailing flat metallicity profiles.

The balance between in situ enrichment by all the stars ever formed at different galactocentric radii and the gas reservoir can give an explanation of the evolution of the gas metallicity profile with the stellar mass in disk galaxies. However, we need to keep in mind that other processes can contribute to shape of the metallicity profiles in these systems: accretion of metal-poor gas leads to steeper metallicity profiles because it produces a metal dilution effect that amplifies the radial metallicity variation (Yates et al. 2021); by contrast, accretion of pre-enriched gas tends to produce flatter metallicity profiles (Fu et al. 2013; Yates et al. 2021); outflows by stellar feedback that mix with the hot halo and fall back into the galaxy disk in the form of galactic fountains with a lower specific angular momentum, triggering radial motions, can steepen the metallicity profiles (Pezzulli & Fraternali 2016); turbulent radial transport, dominant in low-mass systems, can contribute to maintain flat metallicity profiles (Sharda et al. 2021); strong galaxy interactions and major mergers produce almost flat metallicity profiles (Rich et al. 2012).

6. Behaviors of Cluster Galaxies

In Section 4.1 we observed that the metallicity gradients of the cluster galaxies are, on average, flatter than those of field galaxies. In this section we attempt to understand this behavior. Members of galaxy clusters are usually characterized by higher metallicities and gas deficiency with respect to field galaxies (Boselli & Gavazzi 2006; Cooper et al. 2008). These features are interpreted as the result of the suppression of gas accretion, as a consequence of RPS (Gunn et al. 1972), starvation (Larson et al. 1980), or thermal evaporation (Cowie & Songaila 1977). The metallicity profiles of cluster galaxies could be interpreted

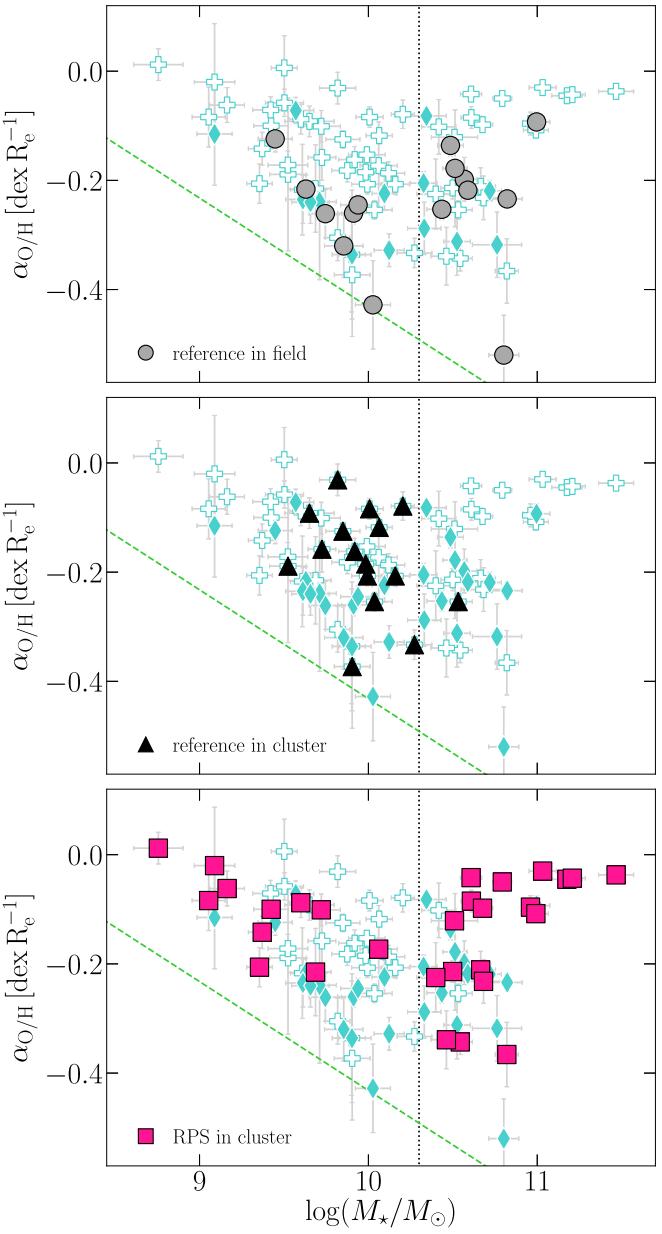

Figure 8. Distribution of the metallicity gradients as a function of the stellar mass. From the top to the bottom panels, we highlight reference field galaxies (gray dots), reference cluster galaxies (black triangles), and stripping cluster galaxies (pink squares), while in each panel, filled elongated diamonds and empty crosses indicate all field and cluster GASP galaxies, respectively, and the vertical line and dashed green line are as in Figure 3.

in the context of the previous section where we discussed that galaxies with a lower gas fraction show shallower metallicity profiles than galaxies with a higher gas fraction and similar mass. Accretion of enriched material is sometimes invoked to explain the behavior of cluster galaxy metallicity profiles (Lian et al. 2019; Schaefer et al. 2019). The accelerated galaxy evolution that occurs in clusters (Guglielmo et al. 2015) might facilitate this flattening. More rarely, confinement pressure exercised by the intracluster medium could prevent the stellar outflows from leaving the galaxy (Mulchaey & Jeltema 2010), making the chemical enrichment of the ISM more efficient.

However, if we take into account the fact that galaxy clusters host various types of galaxy populations, which differ in orbital parameters and time of infall in the halo potential, we cannot simply generalize the behavior of the metallicity gradients observed in cluster galaxies. The GASP sample offers the opportunity to disentangle this issue, as the identification of subpopulations is already provided in many works of the GASP series (e.g., Vulcani et al. 2019b, 2020b; Franchetto et al. 2020).[12] In particular, we use the classification adopted in Franchetto et al. (2020), who study the MZR of three subsamples of GASP galaxies: reference galaxies in clusters (16 objects) and reference galaxies in the field (15 objects)—whose distribution of Hα emission coincides with the stellar morphology and that do not show evidence of gas anomaly features—and cluster galaxies undergoing different stages of RPS (29 objects), clearly identified by the morphology of their Hα emission that presents gas tails and debris or a collimated gas extent unilaterally displaced beyond the stellar disk, whose stellar kinematics is undisturbed. This subselection excludes the field and cluster galaxies whose peculiar morphologies are dealt with in Vulcani et al. (2021) and B. M. Poggianti (2021, in preparation), respectively.

In Figure 8, we explore the distribution of metallicity gradients for these three GASP galaxy categories. Since the stellar mass distributions of these samples are different (Franchetto et al. 2020), we cannot make a robust comparison. However, we can provide general observations. In the top panel we focus on the reference field galaxies: their metallicity profiles steepen with stellar mass up to intermediate masses, while at high masses no clear sequence is detected. In the middle panel, we highlight the reference cluster galaxies: they are distributed in a smaller stellar mass range ($10^{9.5} < M_\star[M_\odot] < 10^{10.5}$) than the other samples, and their metallicity profiles are, on average, flatter than those of field galaxies. In the bottom panel, we consider the galaxies affected by ram pressure stripping: although these galaxies suffer gas removal due to their interaction with the intracluster medium, their metallicity profiles seem consistent with the trend observed for other GASP galaxies and the MaNGA sample, and show a steepening toward intermediate stellar masses and a subsequent flattening at high masses. This indicates that the RPS does not strongly affect the metallicity profiles, since the gas removal occurs on the galaxy outskirts and, then, proceeds outside-in, leaving the gas that is not still stripped mostly unchanged. We also note that most of the massive RPS galaxies host a central active galactic nucleus, whose involved processes might influence their metallicity profile.

The RPS galaxies have most probably fallen only recently into the clusters (<2 Gyr ago) with radial orbits (Jaffé et al. 2018), thus they have experienced the environmental effect only for a relatively short time (typically less than 1 Gyr). This could suggest that their chemical properties are more similar to those of field galaxies with respect to longstanding cluster members. Reference cluster galaxies, instead, could travel on more circular orbits and have felt the influence of the cluster environment on their gas for longer times. To investigate how long ago the reference cluster galaxies entered the cluster, in the top panel of Figure 9 we explore the phase-space diagram (galaxy velocity in the cluster versus the clustercentric distance) of the GASP cluster sample (see also Jaffé et al. 2018 and Gullieuszik et al. 2020). Following Rhee et al. (2017), we highlight the regions where the majority of galaxies lie at a given epoch after they enter in the cluster halo, denoted

[12] Such a detailed distinction is not available for MaNGA.

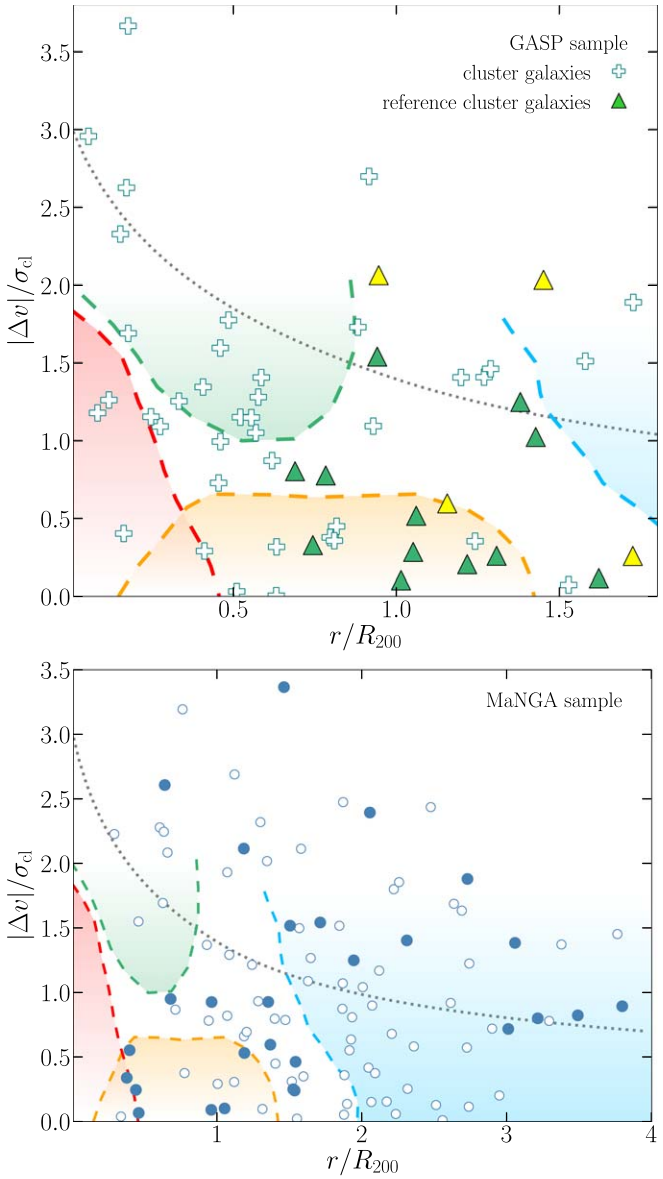

Figure 9. Upper panel: phase space of cluster GASP galaxies. Filled triangles indicate reference galaxies, color coded as in Figure 6 (yellow and green indicate galaxies closer and more distant, respectively, from the line that delimits the forbidden region—Equation (6)). Lower panel: phase space of cluster MaNGA galaxies. Filled dots indicate galaxies with metallicity gradients larger than the 75th percentile. Blue, green, orange, and red shaded areas identify the regions of the diagram mainly populated by first, recent, intermediate, and ancient infallers in the cluster (see the text for details). Gray dotted curve shows the escape velocity in a Navarro et al. (1996) halo assuming a concentration value of 6.

as: first (not fallen yet; blue), recent ($0 < t_{\rm infall} < 3.63$ Gyr; green), intermediate ($3.63 < t_{\rm infall} < 6.45$ Gyr; orange), and ancient ($6.45 < t_{\rm infall} < 13.7$ Gyr; red) infallers. Obviously, these numbers need to be taken with caution and each galaxy can spread out beyond the corresponding region anyway. According to Jaffé et al. (2018) and Gullieuszik et al. (2020), RPS galaxies are mostly located at high velocities and/or low clustercentric distances, i.e., they are preferentially in the regions mainly populated by first and recent infallers, as expected. Instead, reference cluster galaxies have, on average, a low velocity, and are located around the virial radius. They therefore tend to avoid the regions of both recent and ancient infallers, as most of them are placed in the region preferentially occupied by intermediate infallers. Their position in the phase-space diagram supports the idea that these objects have experienced a slow cluster effect for a long time. In addition, as we depict the reference cluster galaxies by the same color code used in Figure 6, it is worth noticing that galaxies with the flattest metallicity profiles (green triangles) are mostly enclosed in the phase-space region dominated by intermediate infallers. By contrast, galaxies with the highest velocities or with the largest clustercentric distances have steeper metallicity profiles for their given stellar mass (yellow triangles), suggesting that they may have fallen in the cluster more recently.

In the bottom panel of Figure 9 we show the phase-space diagram of MaNGA cluster galaxies. This sample includes galaxies at larger virial radii (up to $4\,R_{200}$) than those in GASP and most of them are located in the regions mainly populated by first infallers. In Figure 9, we indicate with filled dots galaxies with shallow metallicity profiles (metallicity gradients greater than the 75th percentile in the stellar bins explored in Section 4.1); we observe that half of these galaxies are concentrated near or inside the region corresponding to intermediate infallers, and thus it is plausible that their flatter metallicity profiles are due to their long presence in the cluster. The other half, instead, spreads above the line of the escape velocity of a Navarro et al. (1996) halo (concentration value of 6); thus, we do not have clues of their nature, even though they could have been pre-processed in groups or merging clusters before entering the main cluster. The above analyses of cluster galaxies in GASP and MaNGA samples are, overall, in agreement, and we find promising hints of a connection between a flat metallicity profile in cluster galaxies and infall time in the host halo.

7. Conclusions

Radial gradients of gas metallicity provide important constraints to understand the formation and evolution of disk galaxies, and their study is attracting a wide attention. In this paper, we have examined a sample of 85 disk galaxies from the GASP survey aiming to investigate the dependence of the ionized gas metallicity gradients on stellar mass and the environment. We also use a larger sample drawn from MaNGA, which allows us to confirm the results obtained using the GASP sample on a more statistical basis and to investigate the role of the gas content in driving the metallicity gradients. The main results can be summarized as follows:

1. The great majority of the observed metallicity gradients are negative, meaning that the central regions are more metal-rich than the outer ones, in agreement with the inside-out formation of galaxies.
2. In both GASP and MANGA, the metallicity profiles are almost flat at the lowest and the highest masses, while steep gradients and a larger scatter are observed at intermediate masses ($\sim 10^{10.3}\,M_{\odot}$).
3. At least up to $10^{10.3}\,M_{\odot}$, the GASP sample shows a clear offset between metallicity gradients of cluster and field galaxies, where the former present flatter profiles than the latter. This difference is also found in MaNGA galaxies at all stellar masses.

Thanks to GASP and MaNGA data, we are also able to study the stellar mass surface density profiles and compare them to the metallicity gradients. We find that:

1. The stellar mass profile steepen with the global stellar mass, in agreement with the findings of previous works.
2. According to the GASP sample, metallicity gradients mildly correlate with the stellar mass gradients (PCC = 0.28); this correlation is the tightest for those galaxies that follow closely the metallicity gradient—stellar mass anti-correlation. Specifically, we do not observe galaxies with flat stellar mass profiles and steep metallicity profiles, while flat metallicity profiles are found in galaxies with steep stellar mass profiles. The median trends of MaNGA galaxies are qualitatively in agreement with GASP, even if the MaNGA sample is characterized by a larger scatter.

This last result suggests that metallicity profiles are initially shaped by in situ star formation that enriched the ISM during the inside-out formation of galaxies, entailing the steepening of the metallicity profiles with the stellar mass. Additionally, mechanisms, mainly dominant at high stellar masses, are at work to flatten the radial distribution of the gas metallicity.

Thanks to the MaNGA data, we are able to study the connection with the galaxy gas content. We find that:

1. For any given stellar mass, the steepness of the metallicity profile correlates with the galaxy gas fraction, i.e., galaxies with flat metallicity gradients have lower gas fraction values than ones with steep gradients.
2. At the same time, as the gas fraction decreases and the metallicity profiles flatten, the metallicity at R_e increases.

The absence of low-mass galaxies with steep metallicity profiles, the correlation between gas metallicity gradients and the stellar mass surface density gradients, and the secondary dependence of the metallicity gradients on the global gas fraction provide important constraints for chemical evolution models.

The dependence on the gas content might be at the origin of the differences between the metallicity profiles of field and cluster galaxies. Indeed, the latter could suffer from suppression of gas accretion according to their orbital trajectory and permanence inside the hostile cluster environment. Our work, carried out both with GASP and MaNGA, suggests that:

1. Cluster galaxies with flatter metallicity profiles have presumably fallen in the host halo sooner than those with steeper profiles. Thus, they have experienced the cluster effect on the infalling gas for a long time. Pre-processing mechanisms can also be involved, and may be statistically identified from the analysis of the phase-space diagram.
2. Metallicity gradients of galaxies undergoing ram pressure stripping do not deviate much from the values found for field galaxies in the considered mass range.

Given the paucity of detailed studies on metallicity profiles of cluster galaxies, we advise additional dedicated works in order to shed light on this class of objects in comparison to field galaxies. To conclude, our results of gas metallicity gradients in disk galaxies can be useful constraints for testing both cosmological simulations and analytical models of galaxy formation and chemical evolution.

We thank the rest of the GASP team for the support and the useful discussions. We thank the anonymous referee for their comments that have improved the paper. Based on observations collected at the European Organization for Astronomical Research in the Southern Hemisphere under ESO program 196.B-0578. This project has received funding from the European Research Council (ERC) under the European Union's Horizon 2020 research and innovation program (grant agreement No. 833824, PI Poggianti). We acknowledge funding from the INAF main-stream funding program (PI B. Vulcani). B. V. and M. G. acknowledge the Italian PRIN-Miur 2017 (PI A. Cimatti). J. F. acknowledges financial support from the UNAM- DGAPA-PAPIIT IN111620 grant, México.

Funding for the Sloan Digital Sky Survey IV has been provided by the Alfred P. Sloan Foundation, the U.S. Department of Energy Office of Science, and the Participating Institutions. SDSS-IV acknowledges support and resources from the Center for High Performance Computing at the University of Utah. The SDSS website is www.sdss.org. SDSS-IV is managed by the Astrophysical Research Consortium for the Participating Institutions of the SDSS Collaboration including the Brazilian Participation Group, the Carnegie Institution for Science, Carnegie Mellon University, Center for Astrophysics | Harvard and Smithsonian, the Chilean Participation Group, the French Participation Group, Instituto de Astrofísica de Canarias, The Johns Hopkins University, Kavli Institute for the Physics and Mathematics of the Universe (IPMU)/University of Tokyo, the Korean Participation Group, Lawrence Berkeley National Laboratory, Leibniz Institut für Astrophysik Potsdam (AIP), Max-Planck-Institut für Astronomie (MPIA Heidelberg), Max-Planck-Institut für Astrophysik (MPA Garching), Max-Planck-Institut für Extraterrestrische Physik (MPE), National Astronomical Observatories of China, New Mexico State University, New York University, University of Notre Dame, Observatário Nacional/MCTI, The Ohio State University, Pennsylvania State University, Shanghai Astronomical Observatory, United Kingdom Participation Group, Universidad Nacional Autónoma de México, University of Arizona, University of Colorado Boulder, University of Oxford, University of Portsmouth, University of Utah, University of Virginia, University of Washington, University of Wisconsin, Vanderbilt University, and Yale University. The MaNGA data used in this work is publicly available at http://www.sdss.org/dr15/manga/manga-data/.

Software: MaNGA data reduction pipeline (Law et al. 2016), MUSE pipeline (Bacon et al. 2010), MaNGA data analysis pipeline (v2.2.1; Westfall et al. 2019; Belfiore et al. 2019b), SINOPSIS (Fritz et al. 2017), KUBEVIZ (Fossati et al. 2016), PPXF (Cappellari & Emsellem 2004), PYQZ (Dopita et al. 2013; Vogt et al. 2015), EMCEE (Foreman-Mackey et al. 2013), FIT3D (Sánchez et al. 2006, 2016).

Appendix A
Stellar Mass Surface Density Profile

Here, we provide an example of the typical stellar mass surface density profile of a GASP galaxy, which we fit to derive the radial gradient. In Figure 10 we show the profile of JO5. The stellar mass radially decreases up to 2 R_e with a linear trend, while at higher radii the profile becomes flat. Within 0.5 R_e, we observe a slight steepening, presumably due to the presence of the bulge. All GASP galaxies have a similar stellar mass profile, where the radius of the outer plateau (if present) can vary between 2 and 4 R_e. Given this common shape of the profiles, we are confident we can obtain a robust estimate of the stellar mass gradient by a simple linear fitting between 0.5 and 2 R_e.

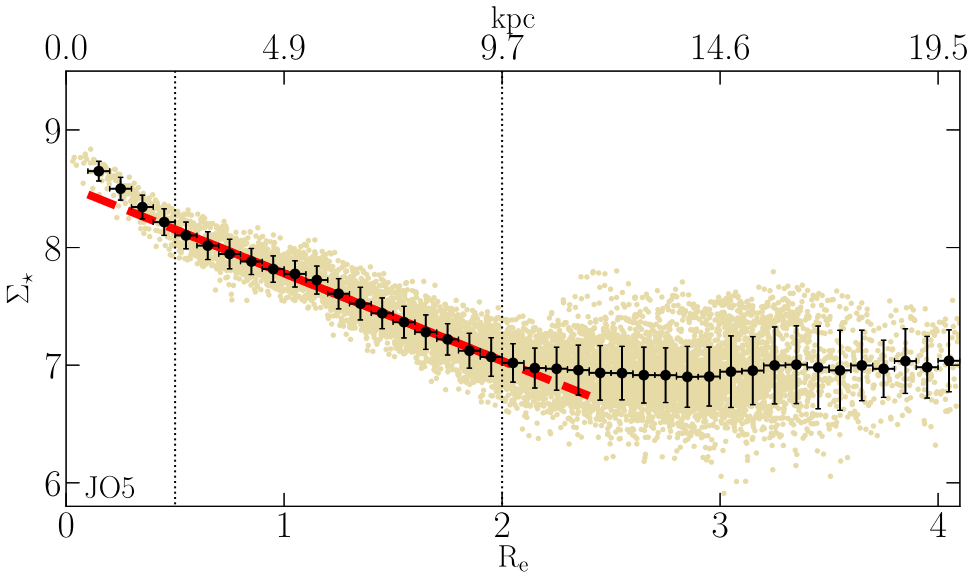

Figure 10. Stellar mass surface density profile of JO5. Small points correspond to the value of each single spaxel, while the black dots are the azimuthal mean in radial bins of 0.1 R_e. The red line indicates the best linear fit between 0.5 and 2 R_e.

Appendix B
Metallicity and Stellar Mass Gradient Values

In Table 1, we provide the properties of the analyzed GASP galaxies and the best-fit gradients of their gas metallicity profiles $\alpha_{O/H}$ and stellar mass surface density profiles $\alpha_{M\backslash *}$, along with the corresponding uncertainties.

Table 1
Properties of the GASP Galaxies

ID	R.A. (J2000)	Decl. (J2000)	env	$\log(M_\star/M_\odot)$	$\alpha_{O/H}$ (dex R_e^{-1})	$\alpha_{M\star}$ (dex R_e^{-1})
(1)	(2)	(3)	(4)	(5)	(6)	(7)
JO73	22:04:25.99	−05:14:47.041	F	$10.0^{+0.1}_{-0.1}$	-0.43 ± 0.08	-0.58 ± 0.09
P11695	10:46:14.89	+00:03:00.838	F	$10.10^{+0.07}_{-0.08}$	-0.22 ± 0.03	-0.76 ± 0.09
P12823	10:52:24.04	−00:06:09.882	F	$10.3^{+0.1}_{-0.1}$	-0.082 ± 0.007	-0.7 ± 0.1
P13384	10:53:03.15	−00:13:30.932	F	$9.9^{+0.1}_{-0.1}$	-0.32 ± 0.06	-0.74 ± 0.07
P14672	11:01:55.10	+00:11:41.095	F	$9.90^{+0.07}_{-0.09}$	-0.3 ± 0.1	-0.67 ± 0.07
P15703	11:06:33.28	+00:16:48.192	F	$11.00^{+0.07}_{-0.09}$	-0.09 ± 0.02	-0.72 ± 0.04
P17048	11:12:38.27	+00:08:01.150	F	$9.6^{+0.1}_{-0.1}$	-0.24 ± 0.04	-0.64 ± 0.07
P17945	11:15:26.45	+00:16:11.586	F	$9.7^{+0.1}_{-0.1}$	-0.26 ± 0.04	-0.64 ± 0.08
P18060	11:14:59.28	−00:00:43.199	F	$9.1^{+0.1}_{-0.1}$	-0.12 ± 0.09	-0.63 ± 0.08
P19482	11:22:31.25	−00:01:01.601	F	$10.33^{+0.07}_{-0.09}$	-0.20 ± 0.02	-0.83 ± 0.07
P20159	11:24:22.26	−00:16:34.268	F	$9.6^{+0.1}_{-0.1}$	-0.07 ± 0.02	-0.57 ± 0.09
P20769	11:27:17.60	+00:11:24.388	F	$9.4^{+0.1}_{-0.1}$	-0.12 ± 0.02	-0.70 ± 0.08
P20883	11:27:45.41	−00:07:16.580	F	$9.9^{+0.1}_{-0.1}$	-0.26 ± 0.02	-0.60 ± 0.08
P21734	11:31:07.90	−00:08:07.914	F	$10.8^{+0.1}_{-0.1}$	-0.52 ± 0.07	-0.87 ± 0.08
P25500	11:51:36.28	+00:00:01.929	F	$10.8^{+0.1}_{-0.1}$	-0.23 ± 0.02	-0.71 ± 0.09
P40457	13:01:33.06	−00:04:51.121	F	$9.7^{+0.1}_{-0.1}$	-0.24 ± 0.04	-0.6 ± 0.1
P42932	13:10:44.71	+00:01:55.540	F	$10.51^{+0.07}_{-0.08}$	-0.2 ± 0.1	-0.70 ± 0.06
P45479	13:23:34.73	−00:07:51.673	F	$10.57^{+0.07}_{-0.08}$	-0.20 ± 0.04	-0.78 ± 0.06
P48157	13:36:01.59	+00:15:44.696	F	$10.59^{+0.08}_{-0.09}$	-0.22 ± 0.02	-0.66 ± 0.08
P5215	10:16:58.24	−00:14:52.876	F	$10.52^{+0.07}_{-0.09}$	-0.31 ± 0.06	-0.70 ± 0.06
P57486	14:11:34.45	+00:09:58.293	F	$9.9^{+0.1}_{-0.1}$	-0.24 ± 0.02	-0.62 ± 0.08
P59597	14:17:41.13	−00:08:39.351	F	$9.7^{+0.1}_{-0.1}$	-0.2 ± 0.1	-0.6 ± 0.1
P63661	14:32:21.78	+00:10:41.428	F	$10.3^{+0.1}_{-0.1}$	-0.29 ± 0.05	-0.75 ± 0.08
P648	10:01:27.74	+00:09:18.372	F	$10.4^{+0.1}_{-0.1}$	-0.25 ± 0.02	-0.60 ± 0.07
P669	10:02:00.62	+00:10:44.299	F	$10.49^{+0.07}_{-0.08}$	-0.14 ± 0.02	-0.75 ± 0.06
P8721	10:34:08.65	+00:00:03.189	F	$10.72^{+0.06}_{-0.07}$	-0.22 ± 0.02	-0.78 ± 0.08
P95080	13:12:08.75	−00:14:20.334	F	$10.1^{+0.1}_{-0.1}$	-0.33 ± 0.03	-0.69 ± 0.09
P954	10:02:03.33	−00:12:49.836	F	$9.6^{+0.1}_{-0.1}$	-0.22 ± 0.03	-0.56 ± 0.09
P96244	14:18:35.47	+00:09:27.828	F	$10.8^{+0.1}_{-0.2}$	-0.32 ± 0.06	-0.72 ± 0.07
A3128_B_0148	03:27:31.09	−52:59:07.655	C	$9.8^{+0.1}_{-0.1}$	-0.12 ± 0.02	-0.8 ± 0.1
A3266_B_0257	04:27:52.58	−60:54:11.565	C	$9.9^{+0.1}_{-0.1}$	-0.16 ± 0.02	-0.62 ± 0.09
A3376_B_0261	06:00:13.68	−39:34:49.232	C	$10.53^{+0.08}_{-0.09}$	-0.25 ± 0.02	-0.84 ± 0.06
A970_B_0338	10:19:01.65	−10:10:36.924	C	$10.06^{+0.07}_{-0.09}$	-0.12 ± 0.02	-0.65 ± 0.09
JO102	03:29:04.69	−52:50:05.364	C	$10.01^{+0.07}_{-0.09}$	-0.08 ± 0.02	-0.6 ± 0.1
JO112	03:40:06.02	−54:02:27.300	C	$9.61^{+0.07}_{-0.08}$	-0.22 ± 0.08	-0.40 ± 0.08
JO113	03:41:49.17	−53:24:13.680	C	$9.7^{+0.1}_{-0.1}$	-0.22 ± 0.08	-0.8 ± 0.1
JO119	06:29:59.10	−54:47:38.690	C	$10.4^{+0.1}_{-0.1}$	-0.10 ± 0.05	-0.7 ± 0.1
JO123	12:53:01.03	−28:36:52.584	C	$9.9^{+0.1}_{-0.1}$	-0.18 ± 0.02	-0.5 ± 0.1
JO128	12:54:56.84	−29:50:11.184	C	$9.9^{+0.1}_{-0.1}$	-0.4 ± 0.1	-0.6 ± 0.1
JO13	00:55:39.68	−00:52:35.981	C	$9.82^{+0.07}_{-0.08}$	-0.30 ± 0.04	-0.61 ± 0.08
JO135	12:57:04.30	−30:22:30.313	C	$10.99^{+0.07}_{-0.08}$	-0.11 ± 0.02	-0.7 ± 0.1
JO138	12:56:58.51	−30:06:06.284	C	$9.7^{+0.1}_{-0.2}$	-0.09 ± 0.03	-0.47 ± 0.09
JO141	12:58:38.38	−30:47:32.200	C	$10.7^{+0.1}_{-0.2}$	-0.23 ± 0.04	-0.71 ± 0.08
JO144	13:24:32.43	−31:06:59.036	C	$10.5^{+0.1}_{-0.2}$	-0.12 ± 0.01	-0.7 ± 0.1
JO147	13:26:49.73	−31:23:45.511	C	$11.03^{+0.07}_{-0.09}$	-0.030 ± 0.004	-0.6 ± 0.1
JO149	13:28:10.53	−31:09:50.200	C	$8.8^{+0.1}_{-0.2}$	0.01 ± 0.03	-0.1 ± 0.1
JO153	13:28:15.15	−31:01:57.859	C	$9.4^{+0.1}_{-0.1}$	-0.07 ± 0.02	-0.5 ± 0.1
JO157	13:28:18.18	−31:48:18.789	C	$10.1^{+0.1}_{-0.1}$	-0.19 ± 0.02	-0.6 ± 0.1
JO159	13:26:35.70	−30:59:36.920	C	$9.8^{+0.1}_{-0.1}$	-0.03 ± 0.03	-0.71 ± 0.08
JO160	13:29:28.62	−31:39:25.288	C	$10.1^{+0.1}_{-0.1}$	-0.17 ± 0.08	-0.76 ± 0.09
JO162	13:31:29.92	−33:03:19.576	C	$9.4^{+0.1}_{-0.1}$	-0.10 ± 0.01	-0.62 ± 0.09
JO17	01:08:35.33	+01:56:37.043	C	$10.16^{+0.08}_{-0.09}$	-0.21 ± 0.02	-0.72 ± 0.07
JO171	20:10:14.70	−56:38:30.561	C	$10.61^{+0.06}_{-0.07}$	-0.08 ± 0.02	-0.3 ± 0.1
JO175	20:51:17.60	−52:49:21.825	C	$10.50^{+0.06}_{-0.08}$	-0.21 ± 0.02	-0.95 ± 0.06
JO179	21:47:07.07	−43:42:18.221	C	$9.5^{+0.1}_{-0.1}$	-0.17 ± 0.03	-0.6 ± 0.1
JO180	21:45:15.00	−44:00:31.188	C	$10.0^{+0.1}_{-0.1}$	-0.18 ± 0.02	-0.65 ± 0.07
JO181	22:28:03.80	−30:18:03.812	C	$9.1^{+0.1}_{-0.1}$	-0.0 ± 0.1	-0.4 ± 0.1
JO194	23:57:00.68	−34:40:50.117	C	$11.2^{+0.1}_{-0.1}$	-0.045 ± 0.009	-0.83 ± 0.07
JO197	09:06:32.58	−09:31:27.282	C	$10.0^{+0.1}_{-0.1}$	-0.25 ± 0.02	-0.68 ± 0.07
JO200	00:42:05.03	−09:32:03.841	C	$10.82^{+0.06}_{-0.08}$	-0.37 ± 0.06	-0.81 ± 0.06
JO201	00:41:30.29	−09:15:45.900	C	$10.79^{+0.05}_{-0.06}$	-0.05 ± 0.01	-0.90 ± 0.08
JO204	10:13:46.83	−00:54:51.056	C	$10.61^{+0.06}_{-0.07}$	-0.042 ± 0.006	-0.75 ± 0.08
JO205	21:13:46.12	+02:14:20.355	C	$9.5^{+0.1}_{-0.1}$	-0.2 ± 0.1	-0.57 ± 0.09
JO206	21:13:47.41	+02:28:34.383	C	$10.96^{+0.04}_{-0.05}$	-0.10 ± 0.02	-0.9 ± 0.1
JO27	01:10:48.56	−15:04:41.611	C	$9.5^{+0.1}_{-0.1}$	-0.06 ± 0.02	-0.6 ± 0.1

Table 1
(Continued)

ID	R.A. (J2000)	Decl. (J2000)	env	$\log(M_\star/M_\odot)$	$\alpha_{O/H}$ (dex R_e^{-1})	$\alpha_{M\star}$ (dex R_e^{-1})
(1)	(2)	(3)	(4)	(5)	(6)	(7)
JO28	01:10:09.31	−15:34:24.507	C	$9.36^{+0.07}_{-0.08}$	-0.21 ± 0.04	-0.47 ± 0.08
JO41	12:53:54.79	−15:47:20.096	C	$10.20^{+0.06}_{-0.07}$	-0.08 ± 0.03	-0.74 ± 0.08
JO45	01:13:16.58	+00:12:05.839	C	$9.2^{+0.1}_{-0.1}$	-0.06 ± 0.03	-0.63 ± 0.08
JO47	01:15:57.67	+00:41:35.938	C	$9.60^{+0.06}_{-0.07}$	-0.09 ± 0.03	-0.43 ± 0.09
JO49	01:14:43.85	+00:17:10.091	C	$10.68^{+0.06}_{-0.06}$	-0.098 ± 0.009	-0.80 ± 0.08
JO5	10:41:20.38	−08:53:45.559	C	$10.3^{+0.1}_{-0.1}$	-0.33 ± 0.03	-0.74 ± 0.08
JO60	14:53:51.57	+18:39:06.364	C	$10.4^{+0.1}_{-0.1}$	-0.22 ± 0.06	-0.6 ± 0.1
JO68	21:56:22.00	−07:54:28.971	C	$10.0^{+0.1}_{-0.1}$	-0.21 ± 0.02	-0.73 ± 0.09
JO69	21:57:19.20	−07:46:43.794	C	$9.9^{+0.1}_{-0.1}$	-0.3 ± 0.1	-0.5 ± 0.1
JO70	21:56:04.07	−07:19:38.020	C	$10.5^{+0.1}_{-0.1}$	-0.34 ± 0.05	-0.95 ± 0.08
JO85	23:24:31.36	+16:52:05.340	C	$10.7^{+0.1}_{-0.1}$	-0.21 ± 0.03	-0.7 ± 0.1
JO89	23:26:00.60	+14:18:26.291	C	$9.72^{+0.07}_{-0.09}$	-0.16 ± 0.04	-0.74 ± 0.07
JO93	23:23:11.74	+14:54:05.013	C	$10.54^{+0.07}_{-0.08}$	-0.34 ± 0.02	-0.86 ± 0.08
JO95	23:44:26.66	+09:06:55.839	C	$9.37^{+0.08}_{-0.09}$	-0.14 ± 0.03	-0.4 ± 0.1
JW10	04:39:18.19	−21:57:49.627	C	$10.0^{+0.1}_{-0.1}$	-0.15 ± 0.01	-0.6 ± 0.1
JW100	23:36:25.06	+21:09:02.529	C	$11.5^{+0.1}_{-0.1}$	-0.04 ± 0.01	-0.68 ± 0.08
JW115	12:00:47.95	−31:13:41.635	C	$9.7^{+0.1}_{-0.1}$	-0.10 ± 0.03	-0.6 ± 0.1
JW29	12:57:49.48	−17:39:57.095	C	$9.50^{+0.07}_{-0.09}$	0.01 ± 0.06	-0.50 ± 0.08
JW39	13:04:07.71	+19:12:38.486	C	$11.21^{+0.07}_{-0.08}$	-0.04 ± 0.01	-0.76 ± 0.08
JW56	13:27:03.03	−27:12:58.205	C	$9.1^{+0.1}_{-0.1}$	-0.08 ± 0.06	-0.6 ± 0.2

Note. Columns are: (1) GASP ID number; (2) and (3) equatorial coordinates of the galaxy center; (4) environment (F = field, C = cluster); (5) logarithm of the stellar mass; (6) gas metallicity gradient; (7) stellar mass surface density gradient.

(This table is available in machine-readable form.)

Appendix C
Best-fit Parameters

In Table 1, we report the best-fit parameters of the functions described in Section 3.3 and adopted to fit the gas metallicity profiles of GASP galaxies.

Table 2
Best-fit Parameters

ID	Function	$\alpha_{O/H}$ (dex R_e^{-1})	Z_{R_e}	R_b (R_e)	R_{in} (R_e)	R_{out} (R_e)	α_{in} (dex R_e^{-1})	α_{out} (dex R_e^{-1})
(1)	(2)	(3)	(4)	(5)	(6)	(7)	(8)	(9)
JO73	dl	-0.43 ± 0.08	8.57 ± 0.04	1.1 ± 0.4	⋯	⋯	⋯	-0.1 ± 0.2
P11695	dl	-0.22 ± 0.03	8.71 ± 0.02	1.5 ± 0.4	⋯	⋯	⋯	-0.03 ± 0.06
P12823	sl	-0.082 ± 0.007	9.112 ± 0.009	⋯	⋯	⋯	⋯	⋯
P14672	dl	-0.3 ± 0.1	8.96 ± 0.03	1.2 ± 0.4	⋯	⋯	-0.07 ± 0.05	⋯
P15703	dl	-0.09 ± 0.02	9.16 ± 0.02	1.3 ± 0.3	⋯	⋯	0.1 ± 0.1	⋯
P18060	sl	-0.12 ± 0.09	8.39 ± 0.04	⋯	⋯	⋯	⋯	⋯
P21734	tl	-0.52 ± 0.07	8.97 ± 0.02	⋯	0.6 ± 0.1	1.8 ± 0.3	-0.05 ± 0.06	-0.1 ± 0.1

Note. Columns are: (1) GASP ID number; (2) best-fit profile function (sl = "single-linear", dl = "double-linear", tl = "triple-linear"; see Section 3.3 for details); (3) gas metallicity gradient; (4) gas metallicity at R_e; (5) break radius of the "double-linear" profile; (6) and (7) inner and outer radii of the "triple-linear" profile, respectively; (8) and (9) inner and outer gas metallicity gradient, respectively.

(This table is available in its entirety in machine-readable form.)

Appendix D
Stellar Mass−Gas Fraction−Gas Metallicity Gradient Surface

In Figure 11, we show the mean distribution of the MaNGA gas metallicity gradients in two-dimensional bins of stellar mass and gas metallicity at R_e (left panel) and in two-dimensional bins of stellar mass and gas fraction (right panel). The values in the two distributions are respectively fitted by a 2nd-order polynomial surface, as described in Section 5.2.

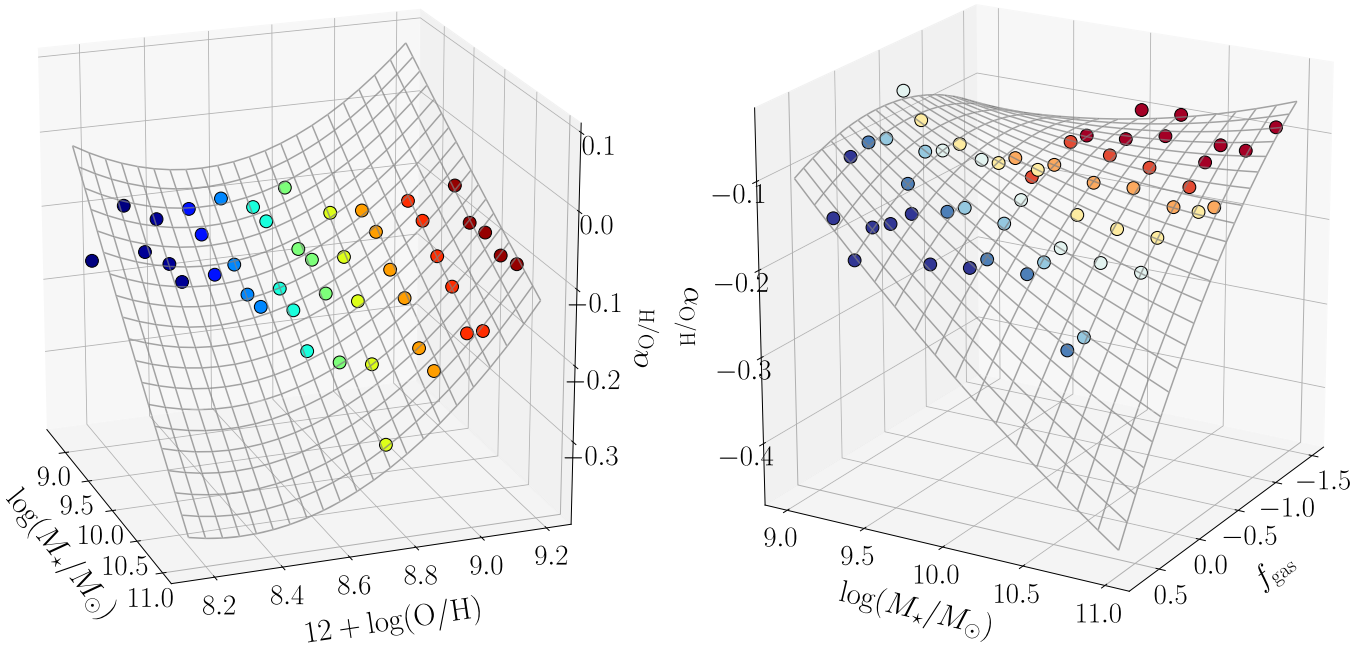

Figure 11. Left panel: distribution of the MaNGA gas metallicity gradients as a function of stellar mass and gas metallicity at R_e. Dots are the mean metallicity gradients in bins of the other two variables, color coded by the gas metallicity, as a guide. The surface is the second-order polynomial fit described by Equation (8). Right panel: distribution of the MaNGA gas metallicity gradients as a function of stellar mass and gas fraction. Dots are the mean metallicity gradients in bins of the other two variables, color coded by the gas fraction, as a guide. The surface is the second-order polynomial fit described by Equation (7).

ORCID iDs

Andrea Franchetto https://orcid.org/0000-0001-9575-331X
Matilde Mingozzi https://orcid.org/0000-0003-2589-762X
Bianca M. Poggianti https://orcid.org/0000-0001-8751-8360
Benedetta Vulcani https://orcid.org/0000-0003-0980-1499
Cecilia Bacchini https://orcid.org/0000-0002-8372-3428
Marco Gullieuszik https://orcid.org/0000-0002-7296-9780
Alessia Moretti https://orcid.org/0000-0002-1688-482X
Neven Tomičić https://orcid.org/0000-0002-8238-9210
Jacopo Fritz https://orcid.org/0000-0002-7042-1965

References

Akaike, H. 1974, ITAC, 19, 716
Ascasibar, Y., Gavilán, M., Pinto, N., et al. 2015, MNRAS, 448, 2126
Bacon, R., Accardo, M., Adjali, L., et al. 2010, Proc. SPIE, 7735, 773508
Baldwin, J. A., Phillips, M. M., & Terlevich, R. 1981, PASP, 93, 5
Belfiore, F., Maiolino, R., Maraston, C., et al. 2016, MNRAS, 461, 3111
Belfiore, F., Maiolino, R., Tremonti, C., et al. 2017, MNRAS, 469, 151
Belfiore, F., Vincenzo, F., Maiolino, R., & Matteucci, F. 2019a, MNRAS, 487, 456
Belfiore, F., Westfall, K. B., Schaefer, A., et al. 2019b, AJ, 158, 160
Bellhouse, C., Jaffé, Y. L., Hau, G. K. T., et al. 2017, ApJ, 844, 49
Bellhouse, C., McGee, S. L., Smith, R., et al. 2021, MNRAS, 500, 1285
Berg, D. A., Skillman, E. D., Croxall, K. V., et al. 2015, ApJ, 806, 16
Berg, D. A., Skillman, E. D., Garnett, D. R., et al. 2013, ApJ, 775, 128
Blanc, G. A., Kewley, L., Vogt, F. P. A., & Dopita, M. A. 2015, ApJ, 798, 99
Blanc, G. A., Lu, Y., Benson, A., Katsianis, A., & Barraza, M. 2019, ApJ, 877, 6
Blanton, M. R., Kazin, E., Muna, D., Weaver, B. A., & Price-Whelan, A. 2011, AJ, 142, 31
Boardman, N. F., Zasowski, G., Newman, J. A., et al. 2021, MNRAS, 501, 948
Boselli, A., & Gavazzi, G. 2006, PASP, 118, 517
Bresolin, F. 2007, ApJ, 656, 186
Bresolin, F. 2015, Mem. Soc. Astron. Italiana, 86, 231
Brown, T., Cortese, L., Catinella, B., & Kilborn, V. 2018, MNRAS, 473, 1868
Bundy, K., Bershady, M. A., Law, D. R., et al. 2015, ApJ, 798, 7
Calvi, R., Poggianti, B. M., & Vulcani, B. 2011, MNRAS, 416, 727
Calzetti, D. 1997, AJ, 113, 162
Cappellari, M., & Emsellem, E. 2004, PASP, 116, 138
Cardelli, J. A., Clayton, G. C., & Mathis, J. S. 1989, ApJ, 345, 245
Carton, D., Brinchmann, J., Wang, J., et al. 2015, MNRAS, 451, 210
Chabrier, G. 2003, PASP, 115, 763
Cid Fernandes, R., Pérez, E., García Benito, R., et al. 2013, A&A, 557, A86
Collacchioni, F., Lagos, C. D. P., Mitchell, P. D., et al. 2020, MNRAS, 495, 2827
Cooper, M. C., Tremonti, C. A., Newman, J. A., & Zabludoff, A. I. 2008, MNRAS, 390, 245
Cowie, L. L., & Songaila, A. 1977, Natur, 266, 501
Cresci, G., Mannucci, F., & Curti, M. 2019, A&A, 627, A42
Cresci, G., Mannucci, F., Maiolino, R., et al. 2010, Natur, 467, 811
Croom, S. M., Lawrence, J. S., Bland-Hawthorn, J., et al. 2012, MNRAS, 421, 872
De Lucia, G., Xie, L., Fontanot, F., & Hirschmann, M. 2020, MNRAS, 498, 3215
De Rossi, M. E., Theuns, T., Font, A. S., & McCarthy, I. G. 2016, BAAA, 58, 24
Debattista, V. P., Roškar, R., & Loebman, S. R. 2017, in The Impact of Stellar Migration on Disk Outskirts, ed. J. H. Knapen, J. C. Lee, & A. Gil de Paz, 434 (Berlin: Springer), 77
Deharveng, L., Peña, M., Caplan, J., & Costero, R. 2000, MNRAS, 311, 329
Dopita, M. A., Sutherland, R. S., Nicholls, D. C., Kewley, L. J., & Vogt, F. P. A. 2013, ApJS, 208, 10
Drory, N., MacDonald, N., Bershady, M. A., et al. 2015, AJ, 149, 77
Ellison, S. L., Simard, L., Cowan, N. B., et al. 2009, MNRAS, 396, 1257
Falcón-Barroso, J., Sánchez-Blázquez, P., Vazdekis, A., et al. 2011, A&A, 532, A95
Fasano, G., Marmo, C., Varela, J., et al. 2006, A&A, 445, 805
Foreman-Mackey, D., Hogg, D. W., Lang, D., & Goodman, J. 2013, PASP, 125, 306
Fossati, M., Fumagalli, M., Boselli, A., et al. 2016, MNRAS, 455, 2028
Franchetto, A., Vulcani, B., Poggianti, B. M., et al. 2020, ApJ, 895, 106
Fritz, J., Moretti, A., Gullieuszik, M., et al. 2017, ApJ, 848, 132
Fu, J., Kauffmann, G., Kauffmann, M.-L., et al. 2013, MNRAS, 434, 1531
Gibson, B. K., Pilkington, K., Brook, C. B., Stinson, G. S., & Bailin, J. 2013, A&A, 554, A47
Giovanelli, R., Haynes, M. P., Salzer, J. J., et al. 1994, AJ, 107, 2036
González Delgado, R. M., Pérez, E., Cid Fernandes, R., et al. 2014, A&A, 562, A47
Grand, R. J. J., Kawata, D., & Cropper, M. 2015, MNRAS, 447, 4018
Grossi, M., García-Benito, R., Cortesi, A., et al. 2020, MNRAS, 498, 1939
Guglielmo, V., Poggianti, B. M., Moretti, A., et al. 2015, MNRAS, 450, 2749
Gullieuszik, M., Poggianti, B., Fasano, G., et al. 2015, A&A, 581, A41
Gullieuszik, M., Poggianti, B. M., McGee, S. L., et al. 2020, ApJ, 899, 13
Gullieuszik, M., Poggianti, B. M., Moretti, A., et al. 2017, ApJ, 846, 27
Gunn, J. E., Gott, J., & Richard, I. 1972, ApJ, 176, 1
Gunn, J. E., Siegmund, W. A., Mannery, E. J., et al. 2006, AJ, 131, 2332
Haffner, L. M., Dettmar, R. J., Beckman, J. E., et al. 2009, RvMP, 81, 969
Hemler, Z. S., Torrey, P., Qi, J., et al. 2021, MNRAS, 506, 3024
Ho, I. T., Meidt, S. E., Kudritzki, R.-P., et al. 2018, A&A, 618, A64
Ho, I. T., Seibert, M., Meidt, S. E., et al. 2017, ApJ, 846, 39
Hurvich, C., & Tsai, C.-L. 1989, Biometrika, 76, 297
Jaffé, Y. L., Poggianti, B. M., Moretti, A., et al. 2018, MNRAS, 476, 4753
Kauffmann, G., Heckman, T. M., Tremonti, C., et al. 2003, MNRAS, 346, 1055
Kewley, L. J., Dopita, M. A., Sutherland, R. S., Heisler, C. A., & Trevena, J. 2001, ApJ, 556, 121
Kewley, L. J., & Ellison, S. L. 2008, ApJ, 681, 1183
Kreckel, K., Ho, I. T., Blanc, G. A., et al. 2019, ApJ, 887, 80
Kreckel, K., Ho, I. T., Blanc, G. A., et al. 2020, MNRAS, 499, 193
Larson, R. B. 1976, MNRAS, 176, 31
Larson, R. B., Tinsley, B. M., & Caldwell, C. N. 1980, ApJ, 237, 692
Law, D. R., Cherinka, B., Yan, R., et al. 2016, AJ, 152, 83
Lian, J., Thomas, D., Li, C., et al. 2019, MNRAS, 489, 1436
Lutz, K. A., Saintonge, A., Catinella, B., et al. 2021, A&A, 649, A39
Ma, X., Hopkins, P. F., Feldmann, R., et al. 2017, MNRAS, 466, 4780
Magrini, L., Vílchez, J. M., Mampaso, A., Corradi, R. L. M., & Leisy, P. 2007, A&A, 470, 865
Maier, C., Hayashi, M., Ziegler, B. L., & Kodama, T. 2019, A&A, 626, A14
Maiolino, R., & Mannucci, F. 2019, A&ARv, 27, 3
Mannucci, F., Cresci, G., Maiolino, R., Marconi, A., & Gnerucci, A. 2010, MNRAS, 408, 2115
Masters, K. L., Stark, D. V., Pace, Z. J., et al. 2019, MNRAS, 488, 3396
Mingozzi, M., Belfiore, F., Cresci, G., et al. 2020, A&A, 636, A42
Moretti, A., Poggianti, B. M., Gullieuszik, M., et al. 2018, MNRAS, 475, 4055
Mulchaey, J. S., & Jeltema, T. E. 2010, ApJL, 715, L1
Navarro, J. F., Frenk, C. S., & White, S. D. M. 1996, ApJ, 462, 563
Osterbrock, D. E. 1989, Astrophysics of Gaseous Nebulae and Active Galactic Nuclei (Sausalito, CA: University Science Books)
Pagel, B. E. J., & Edmunds, M. G. 1981, ARA&A, 19, 77
Peng, Y.-j., & Maiolino, R. 2014, MNRAS, 438, 262
Pérez-Montero, E., García-Benito, R., Vílchez, J. M., et al. 2016, A&A, 595, A62
Pezzulli, G., & Fraternali, F. 2016, AN, 337, 913
Poetrodjojo, H., D'Agostino, J. J., Groves, B., et al. 2019, MNRAS, 487, 79
Poetrodjojo, H., Groves, B., Kewley, L. J., et al. 2018, MNRAS, 479, 5235
Poggianti, B. M., Gullieuszik, M., Tonnesen, S., et al. 2019, MNRAS, 482, 4466
Poggianti, B. M., Moretti, A., Gullieuszik, M., et al. 2017, ApJ, 844, 48
Prantzos, N., & Boissier, S. 2000, MNRAS, 313, 338
Rhee, J., Smith, R., Choi, H., et al. 2017, ApJ, 843, 128
Rich, J. A., Torrey, P., Kewley, L. J., Dopita, M. A., & Rupke, D. S. N. 2012, ApJ, 753, 5
Rupke, D. S. N., Kewley, L. J., & Barnes, J. E. 2010, ApJL, 710, L156
Sánchez Almeida, J., & Dalla Vecchia, C. 2018, ApJ, 859, 109
Sánchez, S. F., García-Lorenzo, B., Jahnke, K., et al. 2006, NewAR, 49, 501
Sánchez, S. F., Kennicutt, R. C., Gil de Paz, A., et al. 2012, A&A, 538, A8
Sánchez, S. F., Pérez, E., Sánchez-Blázquez, P., et al. 2016, RMxAA, 52, 21
Sánchez, S. F., Rosales-Ortega, F. F., Iglesias-Páramo, J., et al. 2014, A&A, 563, A49
Sánchez, S. F., Rosales-Ortega, F. F., Jungwiert, B., et al. 2013, A&A, 554, A58
Sánchez-Menguiano, L., Sánchez, S. F., Pérez, I., et al. 2016, A&A, 587, A70
Sánchez-Menguiano, L., Sánchez, S. F., Pérez, I., et al. 2018, A&A, 609, A119
Schaefer, A. L., Tremonti, C., Pace, Z., et al. 2019, ApJ, 884, 156
Searle, L. 1971, ApJ, 168, 327
Sharda, P., Krumholz, M. R., Wisnioski, E., et al. 2021, MNRAS, 504, 53
Stark, D. V., Masters, K. L., Avila-Reese, V., et al. 2021, MNRAS, 503, 1345
Sutherland, R. S., & Dopita, M. A. 1993, ApJS, 88, 253

Tempel, E., Tamm, A., Gramann, M., et al. 2014, A&A, 566, A1
Tissera, P. B., Rosas-Guevara, Y., Bower, R. G., et al. 2019, MNRAS, 482, 2208
Tomičić, N., Vulcani, B., Poggianti, B. M., et al. 2021a, ApJ, 907, 22
Tomičić, N., Vulcani, B., Poggianti, B. M., et al. 2021b, arXiv:2108.12433
Tremonti, C. A., Heckman, T. M., Kauffmann, G., et al. 2004, ApJ, 613, 898
Vale Asari, N., Couto, G. S., Cid Fernandes, R., et al. 2019, MNRAS, 489, 4721
Valentini, M., Borgani, S., Bressan, A., et al. 2019, MNRAS, 485, 1384
Vogt, F. P. A., Dopita, M. A., Borthakur, S., et al. 2015, MNRAS, 450, 2593
Vulcani, B., Fritz, J., Poggianti, B. M., et al. 2020a, ApJ, 892, 146
Vulcani, B., Poggianti, B. M., Gullieuszik, M., et al. 2018c, ApJL, 866, L25
Vulcani, B., Poggianti, B. M., Jaffé, Y. L., et al. 2018b, MNRAS, 480, 3152
Vulcani, B., Poggianti, B. M., Moretti, A., et al. 2018a, ApJ, 852, 94
Vulcani, B., Poggianti, B. M., Moretti, A., et al. 2019a, MNRAS, 487, 2278
Vulcani, B., Poggianti, B. M., Moretti, A., et al. 2019b, MNRAS, 488, 1597
Vulcani, B., Poggianti, B. M., Moretti, A., et al. 2021, ApJ, 914, 27
Vulcani, B., Poggianti, B. M., Tonnesen, S., et al. 2020b, ApJ, 899, 98
Westfall, K. B., Cappellari, M., Bershady, M. A., et al. 2019, AJ, 158, 231
Wu, P.-F., Zahid, H. J., Hwang, H. S., & Geller, M. J. 2017, MNRAS, 468, 1881
Yates, R. M., Henriques, B. M. B., Fu, J., et al. 2021, MNRAS, 503, 4474
Zaritsky, D., Kennicutt, Robert, C., & Huchra, J. J. P. 1994, ApJ, 420, 87
Zhang, K., Yan, R., Bundy, K., et al. 2017, MNRAS, 466, 3217